Rare earth elements as indicators of post-Marinoan (~635 Ma) paleoceanographic changes from the Amazon Craton

Renan dos Santos, Afonso C.R. Nogueira, Gabriel Uhlein, Fábio Pereira, Guilherme Romero, Pierre Sansjofre, Peter Crockford, Laurane Fogret, Stefan Lalonde

Rare earth elements as indicators of post-Marinoan (~635 Ma) paleoceanographic changes from the Amazon Craton

Renan F. dos Santos[a], Pierre Sansjofre[b], Afonso C.R. Nogueira[ac], Peter W. Crockford[d], Gabriel J. Uhlein[e], Laurane Fogret[b], Fábio S. Pereira[a], Guilherme R. Romero[f], Stefan V. Lalonde[g]

[a] Programa de Pós-Graduação em Geologia e Geoquímica, Faculdade de Geologia, Instituto de Geociências, Universidade Federal do Pará, Rua Augusto Corrêa s/n CEP 66075-110, Belém, PA, Brazil

[b] UMR7590 Institute for Mineralogy, Physics of Materials and Cosmochemistry, Museum National d'Histoire Naturelle, Sorbonne Universite, 75005 Paris, France

[c] Research Productivity of CNPq, Brazil

[d] Department of Earth Sciences, Carleton University, Ottawa ON, Canada K1S 5B6

[e] Universidade Federal de Minas Gerais, Programa de Pós-Graduação em Geologia, CPMTC-IGC, Campus Pampulha, Belo Horizonte, MG, Brazil

[f] Departamento de Geologia Sedimentar e Ambiental, Instituto de Geociências, Universidade de São Paulo, São Paulo, Brazil

[g] CNRS - UMR6538 Laboratoire Geo-Ocean, European Institute for Marine Studies, Université de Bretagne Occidentale, 29280, Plouzané, France

ABSTRACT

The extensive deglaciation linked to snowball Earth climate elapsed in terminal Neoproterozoic caused dramatic changes in the ocean's chemistry, exceptionally recorded in the cap carbonate sequence. One of the most spectacular examples is the post-Marinoan Puga cap carbonate (~635-622 Ma), exposed in the Amazon Craton associated with expressive sea level changes related to the glacial-isostatic adjustment (GIA) resulting in continuous mixed-waters, coastal upwelling succeeded by long-term transgression under greenhouse climax. To better understand the complex dynamics during this period, we conducted a comprehensive multiproxy study encompassing sedimentological, rare earth elements, and stable isotopic analysis. The Rare Earth Element + Yttrium (REY) patterns in the Puga cap carbonate reflect the marine conditions aftermath of the aftermath of the snowball Earth. Specifically, the Y/Ho ratios in the cap dolostones consistently fall below modern seawater values interpreted as seawater composition dilution due to the meltwater influx from the continents during deglaciation. However, superchondritic Y/Ho ratios (up to 70) and positive Eu anomalies (Eu/Eu* up to 3.6) are observed in the basal portion of the cap dolostone. These results suggest the upwelling of hypersaline seawater with some contribution from contemporaneous hydrothermal fluids in shallow coastal water. These findings are interpreted as evidence of ocean destratification related to upwelling, ocean circulation, and glacioisostatic adjustment. The cap dolostone occurs with minimal siliciclastic contributions, consistent with a siliciclastic starvation model. It could be attributed to the persistent shallow-water conditions in the coastal zone, significantly influenced by glacial isostatic adjustment (GIA). This process led to continuous uplift, resulting in a shallow shelf isolated from direct oceanic processes. Barrier-inland facies were not observed in the studied succession, suggesting that irregular diamicton morphologies may have created protected areas against waves. This scenario maintained a consistently shallow water column and followed a significant landward shoreline migration depositional pattern. These dramatic changes have been assumed to have resulted from the rapid recovery of primary productivity during deglaciation, with the proliferation of microbial communities and induced dolomite precipitation. The $\delta^{13}C$ isotopic signature is consistent with these interpretations and with the values found for the Ediacaran in other cap carbonates. Mg concentration was constant during restricted paleoenvironmental conditions on dolomitic platforms. The rapid rise in sea level led to the dispersion of Mg ions, leading to the definitive interruption of dolomicrite precipitation, abruptly replaced by seas supersaturated in $CaCO_3$ with massive aragonite precipitation coinciding with the increase in detrital components under the influence of a long-term transgression in the initial Ediacaran.

Keywords: cap dolostone; starvation siliciclastic, plumeword; restriction; upwelling

1 INTRODUCTION

The transition from the extreme Snowball Earth climate state to more temperate conditions represents a pivotal interval (~720–635 Ma) of Earth's geologic history. These drastic changes were manifested in marine sediments through the dramatic transformation from a globally frozen ocean to an ice-free one (Hoffman et al. 2017, 2021). Significant

perturbations triggered large changes to sea level during the pre-, syn-, and post-glacial stages, primarily driven by the effects of glacial eustasy (global mean sea level), glacial-isostatic adjustment (GIA), and the thermal expansion of the oceans under greenhouse conditions (Allen and Hoffman, 2005; Benn et al. 2015; Creveling and Mitrovica, 2014; Hoffman et al. 2017, 2021, Mitchell et al. 2021, Rame and Marotzke, 2022). During the advance of the syn-deglacial transgression, meltwater production and surface warming created stable density stratification (Yang et al. 2017). Salinity below the meltwater layer, which encompassed the majority of the global ocean at this time, has been estimated to be three times higher than the modern ocean, creating a stable stratification that may have lasted thousands to hundreds of thousands of years (Shield, 2005; Liu et al. 2014; 2018; Yang et al. 2017; Hoffman et al. 2017). The GIA and oceanic circulation were crucial factors for the end of stratification during the post-melting stage (Yang et al., 2017; Rame and Marotzke, 2022).

Globally deposited cap carbonate sequences record a critical interval documenting the transition out of the Marinoan Snowball Earth (Hoffman et al. 2017). These sequences are recognized as the Cryogenian-Ediacaran boundary and consist of basal Ediacaran cap dolostones, which are conformably overlain by cap limestones. These associations exhibit striking similarities across continents and have been globally correlated through geochronological and geochemical means (e.g., Halverson et al., 2005; Corsetti and Lorentz, 2006; Hoffman et al., 2017; Yu et al., 2022).

Current cap carbonate formation models have been proposed to explain the genesis of the Marinoan cap dolostones. In one model, it is suggested that increased seawater alkalinity played a crucial role in the precipitation and widespread dolomitization observed during cap dolostone deposition. These factors include the overturning of deep anoxic ocean waters (Grotzinger and Knoll, 1995; Hoffman et al.,

1998; James et al., 2001), intense chemical weathering (Hoffman et al. 1998; Higgins and Schrag, 2003), Hydrothermal alkalinity model: alkalinity increases linked to extensive hydrothermal activity along basin-bounding faults (Gernon et al., 2016) gas-hydrate destabilization and massive methane release (Jiang et al. 2003, Jiang et al. 2006; Kennedy et al. 2008; Wang et al. 2008), alkanilinity increases associated to microbial activity (e.g., sulfate reduction) (Nogueira et al. 2003,2007, 2022; Font et al. 2006) and meltwater plumes (Shields, 2005; Yang et al. 2017; Liu et al.2014; Santos et al. 2021).

Despite the widespread distribution and intense study of these post-Marinoan sequences and the various proposed models, there has yet to be a consensus regarding their genesis. One aspect that remains to be understood is the microfacies changes from dolostone to limestone. This texture and factory composition transition is key to unraveling the intricate processes during the initial Ediacaran. The precipitation mechanism of cap dolostones remains a subject of intense debate. One reason for these ongoing debates is the variability between units; for example, many units record enigmatic barite horizons (e.g., Bao et al. 2008; Crockford et al. 2016; 2018), while many others do not. Despite this variability, to date, two main hypotheses have been proposed. The first suggests that dolostones formed directly, retaining their primary characteristics and reflecting the chemistry of the original depositional environment (Kennedy, 1996; Shields, 2005; Nogueira et al., 2003; Nedeléc et al., 2007; Font et al., 2006; Santos et al. 2021, 2023). On the other hand, the second hypothesis proposes that the dolostones underwent secondary dolomitization, wherein an aragonite or calcite precursor was transformed into dolomite (Fabre et al. 2013; Higgins et al. 2018; Ahm et al. 2019; Gammon et al. 2012; Gammon, 2012).

Rare earth elements and yttrium (REE+Y) have been extensively utilized in paleoenvironmental and paleoceanographic studies to provide insights into the aftermath

114 of Snowball Earth events (Font et al. 2006; Nedelec et al. 2007, Huang et al. 2009; Meyer
115 et al. 2012; Wang et al. 2014; Viera et al. 2015; Hohl et al. 2015, 2017; Caxito et al. 2018;
116 Verdel et al. 2018; Wu et al. 2019; Zhao et al. 2021; Cui et al. 2021; Ren and Li, 2023)..
117 These elements, when analyzed in ancient non-skeletal carbonates such as microbialites,
118 serve as proxies for reconstructing paleoenvironmental conditions and offer valuable
119 information about past seawater conditions (Schere and Suitz, 1980; Shaw and
120 Wasserburg, 1985; Webb and Kamber, 2000; Kamber and Webb, 2001; Nothdurft et al.
121 2004; Huang et al. 2009; Ling et al. 2013). The incorporation of REE+Y into carbonate
122 minerals is controlled by various physicochemical processes, such as water chemistry,
123 pH, and temperature (Wood, 1990; Nozaki and Alibo, 2003; Chen et al., 2015; Bolhar et
124 al., 2015; Rahlf et al. 2021; Zhao et al. 2022). Consequently, the utility of marine
125 carbonates as recorders of oceanographic conditions hinges upon the preservation quality
126 of these carbonates, well-established diagenetic constraints, and a comprehensive
127 understanding of contamination by noncarbonate phases.

128 Abundant carbonate deposits with well-preserved primary textures occur in the
129 Southern Amazon Craton associated with the Marinoan Puga cap carbonate. Previous
130 studies have predominantly focused on microbial carbonate petrology, sedimentology,
131 and $\delta^{13}C$ and $\delta^{18}O$ geochemical values of carbonates (Nogueira et al. 2003; 2022; Font et
132 al. 2006; 2010; Sansjofre et al. 2011; Soares et al. 2020; Romero et al. 2020; Santos et al.
133 2021,2023). However, despite well-established geological constraints, this succession
134 lacks a comprehensive multiproxy study to constrain the post-Marinoan conditions and
135 test previous carbonate precipitation models, thereby refining our understanding of the
136 factors driving the changes in the carbonate factory over this critical time interval. The
137 evaluation of the Puga cap carbonate exposed in the southern part of the Amazon Craton
138 represents a unique opportunity to achieve this end due to its exceptional preservation,

largely unaffected by severe late-stage diagenetic modification (Sansjofre et al. 2014; Soares et al. 2020; Santos et al. 2021). Therefore, a comprehensive multiproxy study incorporating sedimentological aspects (microfacies and facies), rare earth elements (e.g., Y/Ho, Eu/Eu* and Ce/Ce* anomalies), and isotopic composition of $\delta^{13}C$ and $\delta^{18}O$ may provide the needed insights into the post-Marinoan conditions in this region. For example, the impact of meltwater and stable stratification on ocean circulation in this region and the potential influence of siliciclastic starvation on precipitation and carbonate factory changes (from dolostone to aragonite) remain to be evaluated.

2. GEOLOGICAL BACKGROUND

The focus of this study is the Puga cap carbonate, which is in the Southern Amazon Craton and is associated with the basal deposits of the intracratonic Araras-Alto Paraguai Basin installed during the Late Cryogenian (Fig. 1 A and B). (Nogueira et al. 2003; 2019; Gaia et al. 2017; Afonso and Nogueira, 2018; Santos et al. 2020; Soares et al. 2020; Romero et al. 2020; Santos et al. 2021,2023). This basin overlies crystalline and metamorphic basement rocks of the Cuiabá Group that characterize the Paraguai Belt (Nogueira et al. 2019; Santos et al. 2020). The basal fill of this basin is composed of Cryogenian rocks of the Puga Formation (pelites, sandstones, dropstones, and glacial diamictites) overlain by earliest Ediacaran carbonate rocks of the Araras Group (Fig. 1C), which consists of four formations: 1) Mirassol d'Oeste (Cap dolostone), composed of dolomitic layers interpreted as a shallow platform environment; 2) Guia (Cap Limestone), composed of carbonates and shales, interpreted as a moderately deep platform; 3) Serra do Quilombo, composed of shallow to moderately deep dolomitic platforms; and 4) Nobres, consisting of tidally influenced dolomites (Nogueira and Riccomini, 2006;

Nogueira et al. 2003; 2007; 2019;2022; Rudnitzki et al. 2016; Romero et al. 2020; 2022; Soares et al. 2013; 2020; Santos et al. 2021).

The cap dolostone comprises stratiform stromatolites with gypsum pseudomorphs, giant stromatolites with tubestone, and wave-dominated dolostone facies (peloidal dolomudstone with parallel laminations; peloidal dolopacktone with quasi-planar laminations, and peloidal dolopacktone with megaripples beds). The cap limestone is predominantly composed of limestones with megaripples, wavy laminations, quasi-planar and crystal fans, and subordinate laminated shale (for more details, see Nogueira et al. 2003; 2018; Sansjofre et al. 2014; Soares et al. 2020; Romero et al. 2020; Santos et al. 2021,2023). Post-Marinoan cap carbonate deposition is generally constrained through U-Pb zircon dating and more recent Re-Os dating to between 635.2±0.5 Ma to 632.3±5.9 Ma respectively (Condon et al., 2005; Rooney et al., 2015). Consistent with this are ages of 627±32 Ma for cap dolostone and 622±33 Ma for the cap limestone obtained through Pb-Pb dating, indicating a lower Ediacaran age (Babinski et al. 2006; Romero et al. 2013) and an age of 623 ± 3 [9] Ma U–Pb in situ in seafloor crystal fans was obtained recently by Carvalho et al. (2023). This latter age is interpreted as a new constraint on the transition from shallow to intermediate burial diagenesis of the Puga cap carbonate (Fig. 1C). The isotopic values of $\delta^{13}C$ from -5 ‰ on the hood to -2 ‰ and $^{87}Sr/^{86}Sr$ between 0.7074 and 0.7089 (Fig. 1C) are compatible with global curves (e.g., Otavi Group, Namibia) (Nogueira et al. 2019).

3. MATERIALS AND METHODS

In total, 97 samples were analyzed from the cap dolostone (Mirassol d'Oeste Formation) and cap limestone (Guia Formation) of the Puga cap carbonate, southern Amazon craton (Fig.1). Of these 97 samples, 37 were sampled via outcrop from the Terconi section in the Terconi quarry and 60 were sampled from the Tangará section with

41 samples being taken from drill cores and 19 samples from outcrops (Fig.3 and Fig.4). The samples followed the stratigraphic proposed and facies/microfacies criterion presented by Nogueira et al. 2003; Sansjofre et al. 2014 and Santos et al. 2021,2023.

3.1Trace elements

3.1.1 REE geochemistry - acetic acid leaching

In total, 42 samples of the drillcore JOR, which captures the cap dolostone from the Tangará section, were prepared for major/minor/trace/REE + Y concentrations to avoid REE contributions from non-carbonatic components (e.g., clays and oxides) following the digestion protocol of Rongemaille et al. (2011). Approximately 20 mg of powder was weighed into acid-cleaned 2.5 mL microcentrifuge tubes, and 0.5 mL of trace-metal grade acetic acid at a concentration of 0.85 N (i.e., 5%) was added and left to dissolve the samples overnight at room temperature. Samples were centrifuged, and 0.25 mL aliquots of the supernatant were diluted in 4.75 mL PFA-distilled nitric acid prepared to a concentration of 0.45 N HNO3 (i.e.,2%) with 10 ppb indium as an internal standard to control instrumental drift. Analyses were conducted on a Thermo Scientific ELEMENT XR high-resolution inductively coupled plasma mass spectrometer (HR ICP-MS) of the Pôle Spectrométrie Océan (PSO) at Institut Universitaire Europe´en de la Mer, Université de Bretagne Occidentale, France. Using low, medium, and high-resolution modes allowed for measuring major/minor/trace/REE + Y concentrations at a constant dilution factor during a single analytical session. Repeat analyses of the standard reference material CAL-S (N = 15) showed 1r precision of 7–9%, with results within 10% of published values. Concentrations were determined by external calibration with a synthetic, matrix-matched calibration solution.

3.1.2 REE geochemistry - 2 N nitric acid leaching

In addition, 56 outcrop samples were analyzed, leaching 37 from the Terconi section and 19 from the Tangará section using total bulk dissolution. Rock fragments free of apparent fractures or recrystallization were carefully selected and crushed in an agate mortar. Chemical analysis was performed by ICP-AES (major and minor elements) and ICP-MS (trace elements) at the spectrochemical laboratory (SARM) of the Centre de Recherches en Pétrographie et Géochimie in Vandœuvre-les-Nancy. Samples were prepared by fusion with LiBO2 (980 ◦C during 60 min), followed by dissolution in an HNO3 (1 mol L−1)–H2O2 (∼0.5% v/v)–glycerol (∼10% v/v) mixture to obtain a diluted solution (Carignan et al. 2001). Precision and accuracy were better than 1% of the measured value (mean 0.5%) for major–minor elements and 8% for trace metals, as checked by international standards and analysis of replicate samples (Carignan et al. 2001).

3.2 Stable isotopes ($\delta^{13}C$ and $\delta^{18}O$)

In total, 44 samples of the drill core JOR, which captures the cap dolostone from the Tangará section, were prepared for stable isotope analyses and were performed at the National Museum of Natural History in Paris at the SMIMM Platform. The samples were first ground into a powder in an agate mortar. CO_2 was extracted by dissolution with 100% H_3PO_4 at 70 °C under a primary vacuum. Stable carbon and oxygen isotopic compositions of the product CO_2 were measured using a Kiel IV device. Standards CA21 – Marble – NBS19 were calibrated to the $\delta^{13}C$ sample/ref data. These standards have been calibrated relative to V-PDB using two NBS19 and other international standards. The

results are presented in δ-notation relative to the international Standards V-PDB for $\delta^{13}C$ and $\delta^{18}O$. The external reproducibility for $\delta^{13}C$ and $\delta^{18}O$ measurements is 0.1‰ and 0.15‰, respectively (1σ).

4. RATIONALE FOR THE USE OF RARE EARTH ELEMENTS + YTRIUM (REE+Y) AS PALEOCEANOGRAPHIC INDICATORS

Ancient nonskeletal carbonates, including microbialites, can record ambient seawater rare earth elements and yttrium (REE+Y) concentrations, making them excellent potential archives for paleoenvironment proxies (Schere and Suitz, 1980; Shaw and Wasserburg, 1985; Webb and Kamber, 2000; Kamber and Webb 2001; Nothdurft et al. 2004; Huang et al. 2009; Ling et al. 2013; Hodskiss et al., 2021). However, their utility is predicated on the ability to control for noncarbonate contamination, as well as the impacts of diagenesis (Bolhar and Van Kranendonk, 2007; Rongemaille et al., 2011; Zang et al. 2015; Van Kranendonk et al. 2003; Bolhar et al. 2004; Nothdurf et al. 2004; Olivier and Boyet, 2006; Bolhar et al. 2015). In this study, we primarily utilize Y/Ho ratios, Ce anomalies, and Eu anomalies to explore the post-Marinoan record of the Amazon craton.

The Y/Ho ratio is a geochemical parameter distinguishing between continental and marine influence in marine sediments (Bau et al. 1996; Nozaki et al. 1997; Wang et al. 2014). Yttrium (Y) is more abundant in continental rocks, released during weathering, and transported by rivers. Holmium (Ho) is associated with marine waters (Lawrence et al. 2006). Consequently, the Y/Ho ratio of estuaries shows an increase from crustal values of ~27 to typical marine high values of >40, together with the increasing salinity towards the open ocean (Lawrence and Kamber., 2006). REE + Y is relatively flat in freshwaters with typical Y/Ho values ≈ 26 (Taylor and McLennan, 1985; Kamber et al., 2005;

Lawrence et al., 2006; Bolhar and Van Kranendonk, 2007; Babechuk et al., 2015). Values between ≈ 36 and 26 typically relate to inland waters or mixed seawater-freshwater systems (Webb and Kamber, 2000; Van Kranendonk et al., 2003; Bolhar et al., 2004; Shields and Webb, 2004; Lawrence). Similarly, contamination by detrital components typically overestimates carbonate concentrations of elements such as Al, Ti, Th, and Zr and will reduce Y/Ho ratios to values of ≈27, which is similar to the continental crust and much lower than expected seawater Y/Ho (Webb and Kamber, 2000; Nothdurft et al. 2004; Uhlein et al. 2021).

Ce anomalies are a valuable geochemical tool to assess past redox conditions in sedimentary environments. Cerium (Ce) exists in two oxidation states: Ce (III) and Ce (IV). Ce (III) is preferentially incorporated into sediments in reducing conditions, leading to a higher Ce anomaly, Ce/Ce* >1. Conversely, Ce (IV) is more stable and retained in the sediments under oxic conditions, resulting in a lower Ce anomaly, Ce/Ce* < 1. Ce anomalies in sedimentary records have been widely used to reconstruct marine redox conditions over time (Kamber and Webb, 2001; Bolhar et al., 2004; Bau and Alexander, 2006; Bolhar and van Kranendonk, 2007; Pourret et al., 2008; Planavsky et al. 2010; Ling et al. 2013; Hood and Wallace, 2015; Rodler et al. 2016; Sahoo et al. 2016; Wallace et al. 2017; Zhang and Shield, 2022).

The Eu/Eu* anomaly is a useful indicator for investigating changes in redox and hydrothermal-related parameters (Bau, 1991; Klinkhammer et al., 1994; Barrat et al., 2000; Lawrence et al., 2006; Alexander et al.,2008; Parsapoor et al. 2009). Under reducing conditions, such as hydrothermal systems influence of high-temperature fluids associated with fumaroles, Eu (II) is preferentially incorporated into sediments, resulting in higher Eu/Eu* anomalies. In contrast, Eu (III), under oxidizing conditions, led to lower Eu/Eu* anomalies. High Eu anomalies are absent from the general characteristics of

marine carbonates. The Eu/Eu* ratio in sedimentary records allows us to infer past variations in hydrothermal activity or the presence of Eu in detrital sediments, especially within calcic plagioclase. This insight significantly enhances our understanding of its influence on sediment geochemistry and the resulting shifts in redox conditions over time. (Michard, 1989; Klinkhammer et al., 1994; Haas et al., 1995; Bau and Dulski, 1999; Douville et al., 1999; Barrat et al., 2000; Dai et al., 2016; Liu et al., 2016 Cui et al. 2019).

5. RESULTS

5.1 Major and Trace Elements

Trace element data from the Calcário Tangará and Terconi Quarry sections (Fig. 2 and Fig. 3) are listed in Table 1. They are described below, following the stratigraphic proposed by Nogueira et al. 2003 and Santos et al. 2021,2023. The cap dolostone (Mirassol d'Oeste Formation) was subdivided from base to top into four microfacies: stratiform doloboundstones with gypsum pseudomorph, domic doloboundstones with tubestone, and wave-dominated dolostone facies (peloidal dolograinstone/dolomudstone with quasi-planar laminations and low-angle truncations, and peloidal dolograinstone with megaripples beds) (see Soares et al. 2020, Santos et al. 2021,2023 for more details).

The measured REE+Y data of all Puga cap carbonate samples were normalized to those of post-Archean Australian shale (PAAS) by McLennan, 1989. Anomalies of La, Ce, and Eu were calculated using the equations following (1) Lawrence et al. (2006) and (2) Frimel 2009. Overall, REE+ Yttrium (∑REE+Y) patterns from the Puga cap carbonate are similar in both sections (Fig. 4 and Fig. 5). The Puga cap carbonate shows a progressive enrichment of REEs up section, which is lower than those in the PAAS by less than two orders of magnitude, in the Tangará SectionΣREE+Y: 1.58–60.41 ppm, average = 5.79ppm, n = 61; Fig. 4) and the Terconi Section (ΣREE+Y: 1.4–97.6 ppm, average = 11.4. ppm, n = 37; Fig. 5).

312 **5.1.1. Calcário Tangará Quarry**

313 *5.1.1.1 Cap dolostone from Tangará Quarry*

314 5.1.1.1.1 Microbialites - Tangará Quarry
315

316 In the Calcário Tangará Quarry section (Fig. 2), the microbialites
317 (doloboundstones stratiform stromatolites with gypsum pseudomorph cement and
318 doloboundstones domic stromatolites with tubestone associated) of the cap dolostone
319 showed Mg/Ca ratios ranging from 0.6 to 1.0 (average = 0.8 ± 0.18; n = 42), and low
320 concentration of Sr from 22. to 87 ppm (average = 50 ± 14 ppm) (Fig. 2). The stratiform
321 doloboundstones with gypsum pseudomorphs cement have low concentrations of
322 ΣREE+Y ranging from 1.6 to 27.04 ppm (average = 4 ± 4.7 ppm; n = 32), showed a flat
323 $(REE + Y)_{SN}$ with a depleted LREE pattern (average $(Pr/Yb)_{SN}$ = 1.0 ± 0.3; n= 33) (Fig.
324 6A, C and E). Negative La anomalies, La/La* = 0.8 to 2.2, average = 0.9 ± 0.3). Ce
325 anomalies are mostly weakly negative, with Ce/Ce* = 0.4 to 1.0 (average = 0.9 ± 0.2),
326 and 3) strong positive Eu anomalies, Eu/Eu* =1.0 to 3.2 (average = 1.5 ± 0.5). These
327 facies record slightly super-chondritic Y/Ho ratios (average = 32 ± 10; n = 32), with some
328 sample reaching Y Y/Ho values up to 70 (super-chondritic) (Fig. 7). The Y/Ho ratio of
329 these facies showed an absence of correlation factors (R^2 = 0.023); Th (R^2 = 0.0017); Ni
330 (R^2= 0.0024), and Pb (R^2 = 0.063).

331 The domic doloboundstones with tubestone (giant stromatolites) exhibit ΣREE
332 +Y concentrations between 3.0 to 34.8 ppm (average = 3.7 ± 0.97; n=10) and have a flat
333 $(REE + Y)_{SN}$ (Fig. 4 B) with a depleted LREE pattern (average $(Pr/Yb)_{SN}$ = 0.7 ± 0.97;
334 n =10) (Fig. 6A, C, and E), occurring with 1) Weakly negative Ce anomalies, Ce/Ce*
335 =0.8 to 1.1, (average = 0.9 ± 0.1); 2) Positive Eu anomalies, Eu/Eu*= 1.0 to 1.9, (average
336 =1.3 ± 0.3); and 3) negative La anomalies, La/La*= 0.8 to 1, (average = 0.9 ± 0.1). The

Y/Ho ratio in this location was found to be between 27 and 30 (average = 29 ± 1) (Fig. 7) and shows an absence of correlation factor with Zr (R2 = 0.2); Th (R2= 0.3); Ni (R2= 0.24), and Pb (R2= 0.30).

5.1.1.1.2 Wave-dominated dolostone facies Tangará Quarry

The wave-dominated dolostone facies (peloidal dolomudstone with parallel lamination, peloidal dolopacktone with quasi-planar lamination, and peloidal dolopacktone with megaripples beds) show Mg/Ca ratios ranging from 0.6 to 0.9, (average = 0.6 ± 0.11; n=9) and with low Sr concentrations between 62.75 and 173 ppm (average= 86.4 ± 34 ppm) are similar to those of the basal section (Fig. 2). the concentrations of the detrital component towards the top of the cap dolostone, with Al = 12.34 to 37.88 ppm (average = 25 ± 9.7), Zr =7 to 20 ppm (average =13 ± 5 ppm) and Th = 0.59 to 1.77 (average = 1.18 ± 0.5 ppm) (Fig. 2). The transition from cap dolostone to cap limestone record the decreased purity toward the top of the Puga cap carbonate. The wave-dominated dolostone facies exhibit ΣREE +Y concentrations between 12.3 to 39.02 ppm (average = 26 ppm ± 8.3; n =10), have a flat $(REE + Y)_{SN}$ (Fig. 4C), with a depleted LREE pattern (average $(Pr/Yb)_{SN}$ = 1.0 ± 0.1) (Fig. 6A, C, and E)),. and show the following attributes: 1) Absence of La anomalies La/La* =0.8 to 0.9 (average = 0.84 ± 0.03). 2) weakly negative Ce anomalies Ce/Ce* =0,8 (average = 0.78 ± 0.02), 2). Eu anomalies are small to absent, Eu/Eu* = 0,9 to 1,0 (average=0.96 ± 0.04). Y/Ho = 32 to 34 (average = 33.5 ± 0.6) (Fig. 2) and absence of correlation with Zr (R^2= 0.085); Th (R^2=0.16); Ni (R^2=0.096); Pb (R^2=0.39).

5.1.1.2 Cap Limestone Tangará Quarry

The cap limestone shows higher Sr concentrations between 549 to 1115 ppm (average = 634 ± 196; n =10). The cap limestone is also associated with an elevated

presence of detrital components compared to the cap dolostone, such as Al = 17.15 to 45.42 ppm (average = 34.3 ± 9.3), Zr =18 to 48 ppm (average = 28 ± 10), and Th =1.14 to 2.68 ppm (average = 1.86 ± 0.48) (Fig. 2). Cap limestone has $(REE + Y)_{SN}$ patterns (Fig. 4 D) characterized by a higher concentration of ΣREE +Y, ranging from 34.9 to 60.4 ppm (average = 47.2 ± 8.1; n =10) with a depleted LREE pattern (average $(Pr/Yb)_{SN}$ = 0.87 ± 0.07) (Fig. 6A, C, and E), and show the following attributes: 1) negative La anomalies, La/La* = 0.8 to 0.9 (average = 0.79 ± 0.06); 2) weakly negative Ce anomalies Ce/Ce* = 0.7 to 0.8, (average = 0.76 ± 0.02); 3) Eu anomalies are minor to absent, Eu/Eu*= 0.9 to 1.0, (average =1.04 ± 0.05). The Y/Ho ratio exhibits a super-chondritic value when contrasted with the cap dolostone between 33 to 38 (average = 35 ± 1.6) (Fig. 7) and occurs with an absence of Zr (R^2= 0.069); Th (R^2= 0.35); Pb (R^2= 0.10), and Ni (R^2= 0.13).

5.1.2. Terconi Quarry

5.1.2.1 Cap dolostone from Terconi Quarry

5.1.2.1.1 Microbialites Terconi

The microbialites (stratiform doloboundstones with gypsum cement and domic doloboundstones with tubestone) of the cap dolostone in the Terconi quarry section are similar to those of the Calcário Tangará Section, as follows: 1) Mg/Ca ratio ranging from 0.4 to 0.6, (average= 0.6 ± 0.05; n = 18); 2) low Sr concentrations of between 40 to 60 ppm (average = 49 ppm ± 6; n =17); 3) Zr =1.5 to 12.6 ppm (average = 3.5 ± 3.0); 4) Th = 0.03 to 0.75 (average = 0.19 ± 0.17); and 5) Al = 1.69 to 42.30 ppm (average= 7.9 ± 9.7) (Fig. 3). The microbialites at the basal section occurs with low ΣREE +Y concentrations, ranging from 1.4 to 6.6 ppm (average = 5.80 ppm ± 3.4; n = 18) and have

386 flat (REE + Y) $_{SN}$ patterns (Fig. 5A) with a depleted LREE pattern (average (Pr/Yb) $_{SN}$ =
387 0.82 ± 0.15; n=17) (Fig. 6B, D, and F), and show the following attributes:1) weakly
388 negative Ce anomalies Ce/Ce* = 0.7 to 1.1 (average = 0.93 ± 10), 2) Eu anomalies are
389 small to absent Eu/Eu* = 0.9 to 1.2 (average = 1.08 ± 0.04), and 3) weakly negative La
390 anomalies, La/La* = 0.7 to 1.0, (average = 0.94 ± 0.09). The Y/Ho ratio exhibits a super-
391 chondritic value when contrasted with the medium values of the microbialites from
392 Tangará da Serra, ratios between 32 to 49 ppm (average = 35.2 ± 0.09) (Fig. 3). These
393 ratios showed an absence of correlation with (R^2 = 0.085); Th (R^2 = 0.16); Ni (R^2 = 0.096),
394 and Pb (R^2 = 0.39).

395 5.1.2.1.2 Wave-dominated dolostone facies Terconi

396

397 The wave-dominated dolostone facies (e.g., peloidal dolopacktone with
398 megaripples beds) has Mg/Ca = 0.5 to 0.6 (average = 0.6 ± 0.01 n= 8) and low Sr
399 concentrations similar at the base of the section, between 63 and 87 ppm (average = 59 ±
400 8.4 ppm). In these facies, there is an increase in detrital components compared to the basal
401 microbialites, such as Al = 10.59 to 83.65 ppm (average = 36.6 ± 24.1); Zr = 3.14 to 27.13
402 ppm (average = 12.6 ± 9.25), and Th = 0.24 to 1.54 ppm (average = 0.92 ± 0.55) (Fig. 3).

403 These facies occur with higher ΣREE +Y concentrations than those of
404 microbialites, ranging from 8.32 to 42.26 ppm (average = 15.6 ppm ± 12.5; n = 8) and
405 have flat (REE + Y) $_{SN}$ patterns (Fig. 5B)with a depleted LREE pattern a(average (Pr/Yb)
406 $_{SN}$ = 0.9 ± 0.1; n = 8) (Fig. 6B, D, and F), and show the following attributes:1) weakly
407 negative Ce anomalies, Ce/Ce*= 0.8 to 0.9, (average = 0.87 ± 0.02), 2) Eu anomalies are
408 minor to absent, Eu/Eu* =0.9 to 1.1 (average = 0.95 ± 0.06), and 3) weakly negative La
409 anomalies, La/La* = 0.7 to 1.1, (average = 0.96 ± 0.05) and slightly super-chondritic

410 Y/Ho ratios between 32 to 34 (average = 34.2 ± 1.6) (Fig. 8B) and showed an absence of
411 a correlation between Zr (R^2 = 0.14), Th (R^2 = 0.03), Ni (R^2 = 0.0002) and Pb (R^2 = 0.074).

412 *5.1.2.2 Cap Limestone Terconi Quarry*

413

414 The cap limestone shows higher Sr concentrations between 549 to 1115 ppm
415 (average = 427 ± 347 ppm; n = 12). The cap limestone is also associated with an elevated
416 presence of detrital components compared to the cap dolostone, such as Al = 10.59 to
417 83.65 ppm (average = 71.5 ± 39 ppm), Zr = 63.13 to 194.71 ppm (average = 35.14 ± 17.4
418 ppm) and Th = 1.5 to 3.8 ppm (average =1.8 ± 0.7 ppm) (Fig. 3). Cap limestone has (REE
419 + Y) $_{SN}$ patterns (Fig. 5C) characterized by a significantly higher concentration of ΣREE
420 +Y, ranging from 36,4 to 97,6 ppm (average = 46.3 ± 17 ppm, n =12) with a depleted
421 LREE pattern (average (Pr/Yb) $_{SN}$ = 0.9 ± 0.05, n=12) (Fig. 6B, D, and F), and show the
422 following attributes;1) weakly negative Ce anomalies, Ce/Ce* = 0.9 (average = 0.9 ±
423 0.01); 2) Eu anomalies are small to absent, Eu/Eu* = 0.9 to 1.0 (average = 0.964 ± 0.03),
424 and 3) weakly negative La anomalies La/La* = 0.8 to 1.1 (average = 0.86 ± 0.07). Y/Ho
425 ratios range from 31 to 37 (average = 33 ±2) and show a low correlation between Zr (R^2
426 = 0.29); Th R^2 = 0.47, Ni (R^2 = 0.34) and Pb (R^2 = 8.10^{-6}).

427 5.2 Carbon and oxygen isotope stratigraphy in the Tangará Quarry cap dolostone

428

429 The $\delta^{13}C$ and $\delta^{18}O$ results of the Calcário Terconi Quarry section are presented in
430 Fig. 8 and detailed in Table 2. The isotopic composition is relatively homogeneous. In
431 the dolostone basal (stratiform doloboundstones with gypsum pseudomorphs), $\delta^{13}C$
432 values from -4.1 to - 8.2 (average = -4.8% ± 1.1 n = 33) and $\delta^{18}O$ values from -4.1% to -
433 7.3% (average = -5.1 % ± 0.7 n = 33) occur, followed by $\delta^{13}C$ values from -4.8‰ to

434 −5.7‰ (average = -5.0 % ± 0.3 n = 10) and $\delta^{18}O$ values from -3.7% to - 4.9% (average
435 = -4.7% ± 0.4 n =10) in the domic doloboundstones with tubestone associated. Our data
436 complete the isotopic curve of the dolostone succession (Fig. 7) made by Sansjofre et al.
437 2011 and Nogueira et al. 2019 show an absence of covariation between $\delta^{13}C$ and $\delta^{18}O$
438 (R^2=6.10^{-5}) isotope compositions. The isotopic trends are similar to those obtained for
439 Puga cap carbonates from the southern Amazon craton (Terconi, Fig. 7B) and Calcário
440 Tangará Quarry (Fig. 7A) by Nogueira et al. 2003;2019; Font et al. 2006;2010; Sansjofre
441 et al. 2011, which resemble similar trends for other Ediacaran carbonate platforms.

442 **6. DISCUSSION**

443 6.1 Assessment of detrital input to Puga cap carbonate deposits

444 Previous microfacies studies have suggested that the Puga cap carbonate sequence
445 within the southern Amazon Craton occurs with low detritic content in the matrix,
446 especially the cap dolostone (Nogueira et al. 2003; 2019; Font et al. 2004; Sansjofre et al.
447 2014; Soares et al. 2020; Santos et al. 2021). To assess the impact of detrital contributions
448 on cap dolostone geochemistry (REE+Y anomalies), we evaluated the data using two
449 dissolution techniques: total bulk rock dissolution and an acetic acid leach. The cap
450 dolostone exhibited high purity in both sections, Tangará Quarry (Fig. 2) and Terconi
451 Quarry (Fig. 3); the results are presented below. Our data suggest a clear covariance
452 between the increase in insoluble particles (Zr, Al, Th abundances) vs. ∑REE+Y. Zr
453 concentrations are an excellent marker of siliciclastic contamination, as they are abundant
454 in different detrital materials, and contamination will drive carbonate [Zr] far above
455 typical values of ≈4 ppm (Frimmel, 2009). Similarly, [Th] > 1 ppm may indicate
456 significant contributions from insoluble residues and thus are considered to be another

457 marker of detrital contamination (Webb and Kamber, 2000; Zhao and Zheng, 2014,
458 2017).

459 In this study, binary diagrams were generated to determine the correlation between
460 different element ratios and element concentrations to assess the degree of diagenetic
461 alteration and contamination by siliciclastic materials on ∑REE+Y distribution patterns
462 (Kamber and Webb, 2001; Nothdurft et al. 2004; Bolhar and Van Kranendonk, 2007;
463 Allwood et al. 2010; Wang et al. 2014; Zhao and Zheng, 2014, and Uhlein et al. 2021).
464 Despite the apparent influence on ∑REE+Y, there is a lack of anti-correlation, for
465 example, between Y/Ho ratios, which would be a predicted behavior in carbonates
466 significantly contaminated by terrigenous particles. The increase in the insoluble content
467 of the cap dolostone is observed over the transition from microbialite facies to wave-
468 dominated dolostone (Figs. 2 and 3). Conservative mixing lines between end members
469 are based on Y/Ho vs. (Zr, Th, Al, and ΣREE + Y) (Fig. 8) data using calcite cement from
470 Nothdurft et al. (2004) and PAAS from Taylor and McLennan (1985). The calcite cement
471 by Nothdurft et al. 2004 followed the criterion of purity and not its early diagenetic
472 history.

473 When assessing the impact of detrital materials on total bulk rock dissolution
474 analyses, we find that the cap dolostone is contaminated by 1%–5% detrital particles (Fig.
475 8A and 8B) (Fig. 8E and 8F). However, Y/Ho vs. Al suggests up to <1% contamination
476 (Fig. 8C and 8D), while Y/Ho vs. Th indicates up to 10% contamination (Fig. 8G and
477 8H). Our data display a minimal contribution of insoluble particles in the cap dolostone,
478 especially within the microbialites intervals, and the limestone succession of the cap
479 records the maximum detrital contribution. When analyzing the covariance of detrital
480 components between Y/Ho and Zr and Th, for example, low correlation is demonstrated

481 throughout the succession in total bulk rock dissolution. Another critical factor is that the
482 anomalies remain unaltered, as Y/Ho, Ce/Ce, and Eu/Eu show similarities throughout the
483 entire succession; we further discuss these observations in detail below. However, when
484 applying conservative mixing lines between end members based on Y/Ho vs. Zr, Th, Al,
485 and ΣREE + Y (Fig. 8), the cap limestone displays up to 30% contamination (Fig. 8A and
486 8B) (Fig. 8C, E and F), while Y/Ho vs. Al (Fig. 8 B, C and D) is up to 1% detrital
487 contribution, and Y/Ho vs. Th indicates up to 30% contamination (Fig. 8G and 8H).

488 6.2 Diagenetic influences on the Puga cap carbonate

489

490 Petrographic observations reveal that the matrix of the cap dolostone is
491 predominantly composed of dolomicrite. It consists of replacive micritic pervasive
492 dolomite with irregular intercrystalline boundaries (non-planar) and exhibits bright red to
493 orange luminescence in cathodoluminescence. Texturally, a predominance of the
494 grumose pattern is observed, manifested in diffuse peloids clustered in no individualized
495 micro aggregates or isolated grumous. In rare instances, these peloids partly resemble
496 shrubs, like those described by Frasier and Corsetti (2003). Additionally, replacive
497 dolomite is present in all facies, forming a fine to medium planar-e to planar-s crystal
498 mosaic with sizes ranging from 0.1 to 0.2 mm. The gypsum pseudomorph filling the
499 fenestrae is well-developed. It has sizes ranging from 0.5 to 0.8 mm, occupying the
500 majority of fenestral porosities within the rock, with its occurrence limited to the base of
501 the section. The cement exhibits a fibrous habit, characterized by euhedral crystals that
502 display two distinct growth forms: 1) fascicular and 2) radial/radiaxial, typical of
503 swallowtail twinning. Subordinately, Fe-rich calcites occur mainly in fenestral,
504 interpeloidal, and vug porosity. Furthermore, post-depositional alteration of the cap
505 dolostone primarily occurred through processes such as dolomitization of gypsum,

neomorphism of dolomicrite, development of vugs and intercrystalline porosity, euhedral dolomite precipitation, synsedimentary fracturing, calcite and quartz precipitation, chemical compaction, Fe-Mn-oxide substitution, and precipitation (for more details, see Soares et al. 2020, and Santos et al. 2021; Santos et al. 2023). The diagenetic processes that the cap limestone was subjected to are suggested to have occurred in the following sequence: pyrite precipitation, calcite cementation, neomorphism of micrite and crystal fan, partial crystal fan dissolution, dolomitization, chemical compaction, fracturing, ferrous dolomite and calcite precipitation, pyrite (pseudomorph) and micrite replacement with Fe-oxide and replacement of rhombohedral dolomite by Mn-oxides (Soares et al.2020; Santos et al. 2023).

The paragenetic relationships of the Puga cap carbonate demonstrate consistent evidence of early diagenetic processes, with lesser influence from later mesodiagenetic events (Soares et al., 2020; Santos et al., 2023). The cap dolostone shows a more significant impact of syndepositional cementation, which may have enhanced the preservation of the cap dolostone (Santos et al. 2021., 2023). This exceptional preservation is observed in the well-preserved primary texture and what is interpreted to be primary $d^{13}C$ and $d^{18}O$ signals from the new and previously published data (Nogueira et al. 2003, 2019; Font et al. 2006,2010; Sansjofre et al. 2011; Soares et al.2020, Santos et al. 2021,2023). We discuss possible influences of late fluid-flow interaction in the Puga cap carbonate using mobile trace elements, $\delta^{13}C$, and $\delta^{18}O$ isotopic compositions to evaluate *syn*- or post-diagenetic fluid-rock interactions (Derry, 2010; Brand and Veizer, 1981; Derry et al. 1989; Banner and Hanson, 1990; Jacobsen and Kaufman, 1999; McArthur, 1994; Hohl et al. 2015). The overprint of these fluids can mask the pristine geochemical compositions and thus must be thoroughly monitored (Hohl et al. 2015;2022). All samples analyzed present negative $\delta^{18}O$ values without systematic

correlations with $\delta^{13}C$ values, which is suggestive of the preservation of primary signals (Fig. 9). The low correlation ($R^2 = 6 \times 10^{-5}$) between $\delta^{13}C$ and $\delta^{18}O$ suggests that the carbon isotope system was not significantly disturbed (Folling and Frimmel, 2002). Postdepositional fluids can modify $d^{13}C$ and $d^{18}O$ values (Jacobsen and Kaufman, 1999; Higgins et al., 2018; Crockford et al., 2021). Many mechanisms have been proposed to explain this close covariance in altered $\delta^{13}C$ and $\delta^{18}O$, including early authigenesis in shallow marine sediments (Cui et al. 2017) and post-depositional processes such as interaction with meteoric water and diagenetic fluids during burial diagenesis (Taylor 1977; Banner and Hanson 1999; Knauth et al. 2017; Kennedy, 2009; Zao et al. 2020; Derry, 2010). Therefore, the $\delta^{13}C$ and $\delta^{18}O$ signals of the occurrences of the southern region of the Amazon Craton are interpreted as pristine carbonate, although we acknowledge that the application of additional diagenetic tracers such as $\delta^{44}Ca$, $\delta^{26}Mg$, or $^{\delta7}Li$ would potentially be insightful (Higgins et al., 2018; Ahm et al., 2018; 2019; Crockford et al., 2021). In most samples analyzed, Mg/Ca ratios averaged 0.8 ± 0.18, suggesting that dolomitization partially influenced the succession (Derry et al. 1994). However, the cross plot of $\delta^{18}O$ vs. Mg/Ca shows a low correlation $R^2 = 0.0182$ (Fig. 9), suggesting that late dolomitization processes did not change the values of $\delta^{18}O$ (Lu and Meyers, 1998). This low correlation between Mg/Ca vs. $\delta^{18}O$ and $\delta^{13}C$ vs. $\delta^{18}O$ suggests that isotopes may have maintained pristine signals. Likewise, the low correlation of the Mg/Ca ratio with the Mn/Sr and Fe ratios ($R^2 = 0.015$) indicated that the trace elements did not change during dolomitization (Chen et al. 2022).

Mn/Sr and Sr/Ca variations can have two causes: postdepositional alteration or paleoenvironmental changes. However, our data demonstrated an anti-correlation. The Mn/Sr vs. $\delta^{18}O$ of the cap dolostone showed an absence correlation ($R^2 = 0.017$), and the Sr/Ca vs. $\delta^{18}O$ occurred with $R^2 = 0.43$, while Sr/Ca vs. Mg/Ca occurred with $R^2 = 0.40$.

Despite the low correlation, our data have a more significant relationship with syndepositional dolomitization (Sr/Ca and Mg/Ca) than post-stabilization changes in dolomite (Late diagenesis). Therefore, Mn/Sr and Sr/Ca ratios may result from specific paleoceanographic conditions or the development of alteration processes by diagenetic fluids (Asmerom et al., 1991; Derry et al., 1992; Kaufman et al., 1993; Kaufman and Knoll, 1995; Melezhik et al. 2001Folling and Frimmel, 2002; Halverson et al. 2007). Thus, the high Mn/Sr ratios obtained in many cap dolostones may have been caused by increased Mn concentrations in bottom waters or anoxic porewaters. (Hohl et al. 2017; Chen et al. 2022). Another possible explanation for the high Mn concentration in cap carbonates is that Fe-rich hydrothermal fluids in the coeval anoxic or suboxic deep ocean (Yoshioka et al. 2003; Nédélec et al. 2007; Shen et al. 2005; Font et al. 2006; Hurtgen et al. 2006).

The relationship between our petrographic and isotopic data suggests that diagenetic processes may have occurred due to fluid (possibly seawater) rock interactions during synsedimentary diagenesis or shallow burial (Nogueira et al. 2003; Font et al. 2004; Gilleaudeau et al. 2018; Soares et al.2020; Santos et al.2021,2023). The evidence of early diagenesis demonstrates an early stabilization of the Puga cap carbonate. This evidence is confirmed in the dating of aragonite crystals fans from the cap limestone, which indicates a U-Pb age of 623 million years (Carvalho et al. 2023), suggesting that post-depositional alteration occurred within the first ≈10 million years. In contrast, besides the majority of cap carbonate having the same textural and compositional framework, the diagenetic history seems to be regional and completely dependent on the tectonic, thermal, and burial history of the depositional basins where they were deposited (Soares et al. 2020, Ahm et al., 2019, Santos et al.,2023). However, we suggested that the cap carbonate succession preserves its syndepositional signature. We show that most

post-depositional modifications occurred early, and there is no evidence of effective overprints in the succession. This exceptional preservation qualifies the Puga cap carbonate succession as an excellent candidate for tracing the paleoceanographic dynamics after the Marinoan glaciation.

6.2.1 Diagenetic overprint interference in REE+Y distributions

Previous diagenetic evaluations of the Puga cap carbonate (Soares et al. 2020; Santos et al. 2021) demonstrate a predominance of early diagenesis process, which may have increased the potential preservation of cap dolostone. Diagenetic studies of REE+Y distributions in ancient carbonates suggest that ∑REE+Y patterns may be stable even during relatively intense diagenesis (Webb and Kamber, 2000; Liu et al. 2019) because ∑REE+Y concentrations are low in diagenetic fluids (10^{-6} to 10^{-4} ppm) (Sholkovitz et al. 1989; Banner and Hanson, 1990; McLennan et al. 2003), and the high permeability and porosity of sedimentary carbonates are strongly reduced by calcite cement formation during early diagenesis (Tanaka and Kawabe, 2006).

We analyzed Ce and Eu variations within binary diagrams. Ce and Eu were chosen for investigation due to their high sensitivity to fluid mobilization processes. Ce^{3+} has the potential to oxidize to $Ce^{4+,}$ while concurrently, Eu^{3+} can undergo reduction to Eu^{2+} (Brookins, 1989). Diagenetic overprinting of carbonate deposits will lead to REE enrichment and a decrease in (Dy/Sm). They would show strong covariance between Ce anomalies and $(Dy/Sm)_{SN}$ (German and Elderfield (1990), Shields and Stille, 2001). They could show a positive correlation between Eu/Eu* anomalies and $(Pr/Sm)_{SN}$ (Bolhar and Van Kranendonk, 2007. However, Ce/Ce* anomalies would not covary with $(Dy/Sm)_{SN}$ (Fig. 11), and anticorrelation between Eu/Eu* anomalies and $(Pr/Sm)_{SN}$ suggesting low interference of postdepositional diagenetic fluids in the ∑REE+Y of the

carbonates of the Puga cap carbonate. The Puga cap carbonate sequence shows strong Eu/Eu* anomalies ranging up to 3.2 (average =1.56 ± 0.31). Eu anomalies could be an analytical artifact due to interference by high Ba concentrations during ICP–MS measurements (Jiang et al. 2007). Our data show a low correlation with Ba ($R^2 = 0.35$). Also, the Eu/Eu* anomalies strongly correlate with Gd and Sm ($R^2 = 0.9$), which has nothing to do with isobaric interference with Ba. These positive Eu anomalies can be explained by plagioclase dissolution. Deng et al. (2017) and Langarica et al. (2020) discussed the influences of these variables on Eu anomalies and the flattening of the REE+Y patterns. However, this is not the case in the present study since we demonstrated in section 5.1 the purity of cap dolostone. Our data show low covariance between Eu/Eu anomalies and Zr, Al, and Th. Another possible explanation for the anomalies could be syn- and postdepositional hydrothermal processes because the hydrothermal fluids are a potentially significant secondary flow of REE+Y to the ocean, which carry flat or heavy rare earth (HREE)-depleted REE+Y signal and excessive concentrations of europium (Bau and Dulski, 1996; Douville et al. 1999; Bau e Dulski, 1999; Douville et al. 1999; Barrat et al. 2000; Cui et al. 2019). Furthermore, the previous discussion noted the low covariance of $\delta^{13}C$ vs. $\delta^{18}O$ and the absence of a correlation of Mg/Ca vs. $\delta^{18}O$ (Fig. 9), which suggests minor modification after dolomitization, which agrees with the diagenetic studies by Soares et al. (2020) and Santos et al. (2023). These observations suggest that REE+Y patterns are most consistent with syn or penecontemporaneous processes before cap dolostone stabilization.

6.3 Constraints on the addition of meltwater in shallow platforms during the aftermath of the Marinoan glaciation

The REE + Y patterns of the Puga cap carbonate have distinct shale-normalized patterns compared to modern marine environments, which have uniform LREE depletion

631 and HREE enrichment, positive La anomalies, negative Ce anomalies, and high Y/Ho
632 ratios (Bau and Dulski, 1996; Webb and Kamber, 2000; Kamber and Webb, 2001; Van
633 Kranendonk et al. 2003; Bolhar et al. 2004; Shields and Webb, 2004; Zhang et al. 2016;
634 Tepe e Bau, 2016). The Y/Ho ratio can differentiate between successions influenced by
635 freshwater vs. seawater (Bau et al., 1996; Nozaki et al., 1997; Wang et al., 2014;
636 Hodgskiss et al., 2021). As a result, marine carbonates often exhibit elevated values, i.e.,
637 they are considered superchondritic with Y/Ho ratios > 36 (Bau et al., 1996; Zhang and
638 Nazaki, 1996; Nozaki et al., 1997). Conversely, REE + Y ratios remain relatively constant
639 in freshwater environments, typically hovering around Y/Ho ≈ 26 (Lawrence et al., 2006;
640 Bolhar and Van Kranendonk, 2007). Intermediate ratios are commonly associated with
641 inland waters or mixed systems (Webb and Kamber, 2000; Van Kranendonk et al., 2003;
642 Bolhar et al., 2004; Shields and Webb, 2004; Lawrence and Kamber,2006). However, it
643 has been frequently reported that marine carbonates may exhibit distinct REE + Y
644 patterns compared to seawater, primarily due to the input of freshwater into shallow
645 seawater (Frimmel, 2009; Zhao et al., 2009; Bolhar et al., 2015). Except for Ce, the typical
646 marine rare earth element features can thus be attributed to estuarine or mixing water
647 processes (Lawrence and Kamber, 2006).

The cap dolostone occurs with Y/Ho ratios ranging from 24.50 to 76.67. Our Y/Ho values in the Tangará and Terconi sections are consistent with a mixture of waters leading to an intermediate salinity, for example, in the basal microbialite (stratiform doloboundstones with gypsum pseudomorphs) with an average value of 32 ± 10; n = 32. However, intermittent elevated ratios (up to 70) of typical seawater are observed, implying sporadic episodes of salinity increase (Lawrence and Kamber, 2006). The domic doloboundstone stromatolites with tubestone occur with values between 26 and 33 (average = 29 ± 1), suggesting the mixture of waters (Bolhar and Van Kranendonk, 2007). The wave-dominated dolostone facies (e.g., Peloid dolopacktone with quasi-planar lamination) occur with Y/Ho = 32 to 34 (average = 33.5 ± 0.6) close to marine values coastal. These ratios are common in glacial meltwater and seawater, characterized by generally low Y/Ho values relative to terrigenous REE + Y patterns (Frimmel, 2009; Zhao and Zheng, 2010). These patterns are widely recorded in cap dolostone deposits (REFS). They are commonly interpreted as reflecting the dilution of the seawater signal in shallow marine environments by the influx of meltwater derived from continents in the aftermath of the Marinoan glaciation (~635 Ma). The plume world hypothesis proposed that during the massive Marinoan deglaciation, a thick layer of floating freshwater plume was produced from continental ice melting, creating physical and chemical stratification of the oceans (Shields, 2005; Yang et al., 2017). Upwelling events (e.g., oceanic circulation) disrupt sea stratification (Liu et al., 2014; Rame and Marotzke, 2022). Our mineralogical and geochemical data support this interpretation. During these events, hypersaline deep water reaches shallow water, causing increased salinity, high values of Y/Ho (up to 71), and gypsum precipitation in the fenestral porosities of basal cap dolostone.

6.3.1 Upwelling of hydrothermal and hypersaline fluids in the shallow platform

The Puga cap carbonate exhibits mostly weakly negative Eu anomalies throughout both sequences; however, elevated values are documented at the base of the cap dolostone (microbialites level). High Eu anomalies are absent from the general characteristics of marine carbonates (Lawrence et al. 2006) and are generally regarded as strong indicators of high temperature-reducing fluids (Bau, 1991; Klinkhammer et al. 1994; Barrat et al. 2000; Alexander et al.,2008; Parsapoor et al. 2009. REE-depleted patterns with positive Eu anomalies indicate the contribution of hydrothermal fluids (Cui et al. 2019). Our data are consistent with positive Eu/Eu values, which are generally considered a sign of hydrothermal components in previous studies of post-Marinoan cap dolostones (Font et al. 2006; Nédélec et al. 2007; Huang et al. 2011; Meyer et al. 2013; Wang et al. 2014; Rodler et al. 2016; Hohl et al. 2017; Xiao et al. 2020).

We tested the hydrothermal influence on cap carbonates using Fe/Ti vs. Al/ (Al + Fe + Mn) (Bostrom, 1973; Barrett, 1981). Deposits with a strong hydrothermal influence don´t typically occur with high concentrations of Al, resulting in high Al/Ti ratios (Marchig et al. 1982). The contamination of these deposits by pelagic and terrigenous seabed sediments enriches them in components such as Ti and Al, resulting in a drastic reduction of Fe/Ti ratios and an increase in the Al/ (Al + Fe + Mn) ratio. High FeT/Al ratios but deficient concentrations of extractable pyrites suggest ferruginous rather than euxinic conditions (Huang et al. 2011). In addition, REE absorption by Fe oxides is typically associated with submarine hydrothermal plume activity (German et al. 1991; Ling et al. 2013).

Our data suggest a robust hydrothermal influence with respect to siliciclastic contamination (Fig. 10A). The Eu/Eu anomalies are strongly correlated with Fe/Al ratios (Fig. 10B). This relation of the increase in Fe accompanying the strong Eu anomalies reinforces the interpretation of a hydrothermal contribution for the Puga cap carbonate, similar to what was described by Jing Huang in 2011, which suggests a hydrothermal origin of elevated iron and manganese for the Doushantou cap carbonate from China. Furthermore, we assessed the hydrothermal impact by applying conservative mixing lines (see Fig. 10 D, E, and F). This approach aligns with the model proposed by Alexander et al. (2008), which considers the interaction of high T-hydrothermal fluids with seawater during sediment deposition using the MREE/HREE ratios. To achieve this, we integrated data from high T-hydrothermal sources (>350 °C, as per Bau and Dulski, 1999) and shallow seawater components (as per Alibo and Nozaki, 1999). Conservative mixing calculations between end members based on Sm/Yb vs. Eu/Sm (Fig. 10 D) indicate that a high-T hydrothermal fluid contribution of less than 1% could have been responsible for the anomalies recorded in the cap dolostone (Alexander et al. 2009). The Eu anomalies and the strong Sm/Yb and La/Yb ratios suggest interaction with hydrothermal syndepositional fluids (Fig. 10). The studied samples were plotted distant from the mixing line (between 0.1 and 1% hydrothermal fluids). This scenario suggests no influence of high-temperature fluids and that the depositional environment of carbonate rocks was distant from fumaroles. However, positive Eu anomalies obtained from Archean and Paleoproterozoic chemical sediments are interpreted as mixtures of seawater and hydrothermal fluids (Kamber and Webb, 2001; Frei et al., 2008; Hodgskiss et al., 2021). For the Ediacaran, positive Eu anomalies are typical for the deep anoxic ocean (Kamber and Webb, 2011; Bolhar et al., 2005; Allwood et al., 2010; Rodler et al., 2016). In addition, our interpretations are similar to recent interpretations for the origin of the

Doushantou cap carbonates, which are mainly based on $\delta^{13}C$, $\delta^{34}SCAS$, $\delta^{17}O_{CAS}$ $\delta^{44}Ca$, $^{87}Sr/^{86}Sr$, rare earth, elements, and metal trace elements. These data suggest that they may have been formed under the influence of deglacial meltwater, hydrothermal fluids, and upwelling (Huang et al. 2009; Huang et al. 2011; Huang et al. 2013; Wang et al. 2014; Hohl et al. 2017; Zhao et al. 2018; Wei et al. 2019a; Peng et al., 2022).

Carbonates associated with deep ocean brine are characterized by Fe and trace metal enrichments with positive Eu anomalies (Meyer et al. 2012). Liu et al. (2013) extensively discussed the potential origin of radiogenic $^{87}Sr/^{86}Sr$ in Marinoan cap carbonates of the Nuccaleena Formation, South Australia. They found that the interaction of the carbonates with brines or hydrothermal fluids could better explain these values, or they may reflect values from glacial meltwater mixing with seawater. This evidence strengthens previous interpretations that the Marinoan cap carbonate precipitated in a mixture of coastal meltwater with saline Mg-rich deeper waters through the upwelling process (Grotzinger and Knoll, 1995; Ridgwell et al., 2003; Shields, 2006; Yang et al., 2017; Liu et al. 2014;2018; Hoffman et al. 2017; Santos et al. 2021; Rame and Marotzke, 2022). Through modeling, a glacial hydrothermal flow during the Marinoan snowball glaciation was demonstrated using a binary mixture of Ge/Si and Eu/Eu* values (Cui et al., 2016). Marinoan deposits were accumulated during the drifting stage of post-rift subsidence (Hoffman et al. 2017), and this hydrothermal flow during Snowball Earth events could potentially enrich the oceans in certain elements in the aftermath of the Marinoan glaciation.

The syndepositional hydrothermal event was unlikely, and these observations align with our interpretations of rapid precipitation of the Marinoan cap carbonate (Hoffman et al. 1998; Nogueira et al. 2003; 2019; Cui et al.2016 Zhou et al. 2019; Santos et al. 2021). Our data suggests some samples with typical seawater values (Y/Ho up to

745 70) others displaying strong indications of hydrothermal fluid interaction (Eu/Eu* up to
746 3.2). Nevertheless, most of our samples exhibit Y/Ho ratios typical of mixwater,
747 approximately ~ 33 (a combination of glacial meltwater and seawater). This finding aligns
748 consistently with interpretations of upwelling events during the precipitation of the cap
749 dolostone. These deep Cryogenian waters would have interacted with high-temperature
750 hydrothermal fluids responsible for the elemental enrichments (e.g., Eu, Fe, Mn). At this
751 time, deep waters would have interacted with high-temperature hydrothermal fluids
752 responsible for the elemental enrichments (e.g., Eu, Fe, Mn). This evidence is consistent
753 with the diachronous precipitation model for the Marinoan cap dolostone from the melt-
754 water layer during syn-deglacial transgression (Hoffman et al. 2017).

755 This upwelling interaction may have also lowered the Y/Ho values of the
756 dolostone samples in the basal succession, as hydrothermal fluids tend to possess low
757 Y/Ho ratios. (Allwood et al. 2010). In addition, as discussed in section 5.1, we
758 demonstrated the absence of interference of siliciclastic components at lower Y/Ho
759 values. The base of the cap dolostone shows a fluctuation in the Y/Ho values and high
760 values of Eu anomalies, suggesting a strong contribution from hydrothermal sources of
761 REE+Y to the cap dolostone of the southeast margin of the Amazon Craton.

762 6.4 Paleoredox indications

763 Ce/Ce* anomalies in the Puga cap carbonate indicate oxygen deficiency
764 throughout the section (Fig. 11), but these anomalies are weaker in the microbialite
765 interval. In modern seawater, REE+Y (Rare Earth Elements + Yttrium) can record the
766 evolution of seawater redox, and the negative Ce anomaly marks oxidized conditions
767 (Byrne and Sholkovitz, 1996; Webb and Kamber, 2000; Ling et al., 2013), while the
768 absence of anomalies is indicative of anoxic conditions (Lawrence et al., 2006).
769 Furthermore, soluble Ce^{3+} is easily oxidized to Ce^{4+}, which is relatively insoluble in oxic

seawater (McLennan, 1989; Alibo and Nozaki, 1999; Pattan et al., 2005; Frimmel, 2009). Therefore, the Ce anomaly in marine sediments distinguishes oxic from anoxic depositional environments throughout the sedimentary record (Bau et al., 1996; de Baar et al., 2018).

However, the scenario presented thus far demonstrates the influence of water mixing, particularly a strong influence of meltwater. The Y/Ho ratio exhibited similar behavior to estuarine dynamics (freshwater and saltwater). Except for Ce, typical marine rare earth element features can be attributed to estuarine or mixing water processes since Ce anomalies only form in salinities greater than 2% (the ocean average is 3.5%) (Lawrence and Kamber, 2006). Therefore, only samples with a Y/Ho ratio ≥ 36 will be considered for interpretation. Three samples fall into the oxygenated category, but most of these eligible samples exhibit values suggesting dysoxic conditions. Our results have been extensively tested for post-depositional changes; at least, the samples with high Y/Ho ratios may reflect the redox conditions of our post-Marinoan scenario.

The interpretation of a dysoxic to anoxic water environment in the Puga cap carbonate is consistent with other post-Marinoan deposits (Huang et al., 2009; Huang et al., 2011; Wang et al., 2014; Lang et al., 2016; Rodler et al., 2016; Hohl et al., 2017; Caxito et al., 2018; Wu et al., 2019; Hu et al., 2023; Ren and Li, 2023). In this sense, it could reflect the biochemical conditions of this anomalous environment, as Ce anomalies are known to be affected by environmental parameters such as pH, alkalinity, and microbial activity (De Baar et al., 1985a; Alemão and Elderfield, 1990; Byrne and Kim, 1993; Pourret et al., 2008; Zhao et al., 2022). The Ce/Ce* values of the studied samples (0.70–1.05, mostly below 0.95) could indicate a small amount of oxygen deficiency in the water column (Fig. 11). Dysoxic waters would have likely provided even more stressful conditions for microbial life after the Marinoan glaciation. Generally, oxidizing

795 conditions prevailed in the atmosphere and shallow seawater during the post-Marinoan
796 phase (Fike et al., 2004; Sahoo et al., 2012; Sansjofre et al., 2014; Hohl et al., 2015; 2017;
797 Wy et al., 20xx; Ader et al., 2014). Sansjofre et al. (2014), based on trace metals,
798 suggested that a water column must have been essentially oxic during the cap dolostone
799 precipitation, with anoxia only sporadically reaching the sediment–water column
800 interface in the deepest parts of the platform on the Amazon craton. The interpretation of
801 these authors differs in part from our findings, which indicate predominantly dysoxic
802 water. However, other proxies must be applied to understand microbial communities' role
803 and evaluate the reservoir effect due to water mixing.

804 6.5 CAP CARBONATE PRECIPITATION MODEL AND GLOBAL CORRELATION

805 The cap carbonate immediately precipitated over the Puga diamictite in a coastal-
806 marine environment influenced by microbial mat proliferation during the transition from
807 icehouse to greenhouse conditions(Nogueira et al. 2003; 2019; 2019; Font et al.
808 2006,2010 Nédélec et al. 2007; Sansjofre t al. 2014; Santos et al. 2021,2023). The
809 deformed dolomite-diamictite contact indicates rapid accumulation of dolomicrite
810 deposited over a still plastic diamicton linked to a regional scale event compatible with
811 the glacial isostatic adjustments on the coastal zone, forming a substrate with irregular
812 morphology (Nogueira et al. 2003;2019). Rapid precipitation ($\approx 10^3 - 10^4$ years) for cap
813 dolostones is consistent with our sedimentological evidence and other models, such as
814 enhanced continental weathering alkalinity addition, gas hydrate destabilization, and
815 persistent freshwater surface layer (Shields, 2005; Hoffman et al., 2017; Crockford et al.
816 2021). Complete glacier retreat and ocean warming were succeeded by isostatic
817 adjustments, characterized by an uplift of continental areas and eustatic subsidence on the
818 coastal zone, concomitant with relative post-glacial sea-level rise (Creveling and
819 Mitrovica, 2014) and during the advance of the syn-deglacial transgression, meltwater

production and surface warming created stable density stratification (Liu et al. 2014;2018; Yang et al. 2017; Hoffman et al. 2017). The diamicton substrate was colonized by microbial communities in stratified and shallow water, and the high organic productivity due to the maximum nutrient input from mixed water culminated in the giant biostromas built on the coast (Santos et al. 2021). The microbial communities that colonized the diamicton recorded not only the influences of the chemistry of the environment but also the effects of the hydrodynamics of the environment. According to Yang et al. (2017), water stagnation and high density led to the development of lamination (Santos et al. 2021).

The negative $\delta^{13}C$ isotope signatures can be considered a consequence of microbial activity, producing organically derivatived ^{13}C-depleted bicarbonate (Nedeléc et al. 2007). These interpretations are consistent with our $\delta^{13}C$ data ranging from −8.2‰ to −4.1‰ (average = -4.9%); as discussed earlier, our tests suggested values that express Early Ediacaran seawater chemistry, as well as previous data for Puga cap carbonate (Nogueira et al.2003;2019; Fonte et al. 2006; Sansjofre et al. 2011) similar to Marinoan cap dolostone successions worldwide (Nedeléc et al 2007; Hoffman et al., 2021; Peng et al., 2022). Thus, the negative carbon isotope values may reflect the high productivity after the Marinoan glaciation in a dysoxic water column, with intense microbial activity on the paleocoast due to rising temperatures and significant inputs of nutrients provided by reactivation of ocean biogeochemical cycling and an increased hydrological cycle (Kunzmann 2012; Sansjofre et al. 2014; He et al. 2021). These conditions favored the proliferation and preservation of a giant biostroma laterally continuous for kilometers in the paleocoast (Nogueira et al. 2003;2022; Font et al. 2006; Romero et al. 2020; Santos et al.2021,2023).

844 During deglaciation, continental ice sheets trapped detrital materials (Hoffman et
845 al. 2017; Yu et al. 2020). Estimating how long the sediments were trapped in the ice sheets
846 in the distal zone before reaching the coastal area is impossible. However, rapid
847 precipitation for cap dolostones is consistent with our sedimentological evidence. Our
848 data show intense participation with microbial activity (giant stromatolites), an abrupt
849 increase in alkalinity (cap dolostone-cap limestone transitions), plume world (Mixwater
850 and gypsum cement), and siliciclastic starvation (pure carbonates). Rapid precipitation is
851 consistent with other models, such as continental weathering alkalinity, gas hydrate
852 destabilization, and plume world, as well as sedimentary features and geochemical
853 models (~10^3 –10^4 years) (Shields, 2005; Crockford et al., 2016; Hoffman et al., 2017;
854 Yang et al., 2017; Crockford et al. 2021). However, a single model does not explain the
855 precipitation of the Puga cap carbonate despite the similarity between different sequences
856 of this age. A reason for this heterogeneity is that there is an endemic distinct preservation
857 between locations, primarily related to the paleogeographical position that dictates the
858 coastal/marine dynamics.

859 We have previously demonstrated the purity of cap dolostone, between 1 and 5%
860 contamination, based on Y/Ho vs. Zr and Al (see item 5.1). These conditions of high
861 density, up to 3 times higher than current rates, according to the model by Yang et al.
862 2017, may have controlled the sediment inflow to the shallow carbonate platform,
863 indicated by the low content of detrital components in the cap dolostone (figs). The
864 density between meltwater and seawater or even sediment starvation can explain the low
865 content of detrital constituents. The starvation of sediments indicates precipitation of the
866 cap dolostone over ~10^5 – 10^6 years (Spence et al. 2016; Wallace et al. 2019). A larger
867 landward shoreline migration in the siliciclastic starvation model in cap deposition is not
868 directly associated with final Snowball Earth conditions (Nordsvan et al. 2019). During

deglaciation, detrital materials were trapped in continental ice sheets (Hoffman et al. 2017; Yu et al. 2020). In modern shelves, the area starved of sediment is associated with detritic trapping that can occur at the terrestrial limit with the saline wedge, producing maximum estuarine turbidity (Swift, 1968; Kidwell, 1991; Geye et al. 2004; McHugh et al., 2010). The generation of hyperpycnal flows to transport fine sediments distributed in surficial plumes that only occur in very shallow waters can extend for thousands of kilometers (Geyer et al. 2004; Dowdeswell et al. 2015. The model by Yang et al. (2017) postulates a salinity three times higher than the current level. In this sense, the detrital content in meltwaters from the Marinoan deglaciation could be trapped during the linkage of freshwater and hypersaline seawater, forming extensive plumes with thousands of kilometers.

However, our geochemical data does not agree with a higher salinity during fast cap dolostone precipitation in mixwaters as previously demonstrated (Y/Ho ratios of the mixwater patterns). Another possible explanation for siliciclastic starvation could have arisen due to the restricted conditions with persistently shallow waters in the coastal zone. This depositional scenario was strongly influenced by glacial isostatic adjustment (GIA) or rebound but affected only the initial meters of cap dolostone (e.g., Nogueira et al. 2003). This process led to continuous uplift in conjunction with a rapid post-glacial sea-level rise, maintaining a shallow shelf isolated from direct oceanic processes. Barrier-inland facies were not observed in the studied succession, indicating that irregular diamicton morphologies may have created protected areas against waves, promoting stratiform microbial proliferation and inducing dolomite precipitation. This scenario resulted in a consistently shallow water column, following a significant landward shoreline migration depositional pattern with a high potential for preserving the same

893 signature, devoid of detritic components, found for hundreds of kilometers along the
894 southern margin of the Amazon Craton.

895 The conditions outlined above likely lasted for approximately ~8 ka (Liu et al.
896 2014) or would have occurred on a scale of 10^4 and 10^5 years following a unidirectional
897 mixing model associated with thermal expansion (Yang et al. 2017). Another hypothesis
898 suggests only a few thousand years for the mixing waters based on a three-dimensional
899 model considering oceanic circulation as a crucial factor for the end of stratification by
900 meltwater (Rame and Marotzke, 2022). Although the glacial-isostatic adjustment (GIA)
901 could be the driving force influencing the mixing of the waters and paleoceanography,
902 the time spent developing this event depends on the ice cap thickness and melting
903 velocity. The lack of terrigenous components in cap dolostone may be evidence of rapid
904 precipitation (keep-up) before the main detritic flow on the coast of the Amazon craton
905 or lasted at least as long as the stratified oceans.

906 6.6 Implications for the Carbonatic Factory Change

907

908 Water turbidity increases partially inhibit carbonate precipitation, causing marl
909 deposition and suppressing microbial life, a prelude to marine stratification declines and
910 thermal expansion (Romero et al. 2020; Santos et al. 2021; Nogueira et al. 2022). The
911 mixing waters and massive detritic flow generated a geochemical change, causing CaCO3
912 over-saturation, which contributed to the precipitation of poloidal limestones with calcite
913 crystal fans (pseudomorphs after aragonite) (Higgins and Schag, 2003; Nogueira et al.
914 2003, 2007, 2019; Hoffman et al. 2017,2021; Soares et al. 2020; Santos et al. 2021,2023).
915 The cap limestone presents an abrupt increase in the Sr concentration that accompanies a
916 rise in Zr, Al, and Th in covariance with REE+Y), indicating a direct relationship between

917 the siliciclastic input and the increases in alkalinity and, as a consequence, a change in
918 the dolomitic-aragonitic features.

919 Our geochemical and microfacies data support an abrupt transition in the carbonate
920 factory, as enhanced continental weathering could have lowered seawater Mg/Ca ratios
921 with substantial input of Ca2+ to platform environments (Hoffman et al.1998, xx),
922 triggering CaCO3 oversaturation (Nogueira et al. 2019). Marine chemistry changes are
923 commonly associated with secular modifications such as the Mg/Ca ratio, pH, redox state
924 of the ocean, climate (icehouse-greenhouse conditions), pCO2, and the extent of
925 continental weathering (Hardie, 1996, 2003; Hood and Wallace, 2018; Ries, 2010;
926 Sandberg, 1983; Stanley and Hardie, 1998; Wood et al., 2017; Wey et al., 2022). The cap
927 dolostone-cap limestone transition saw an increase in the concentration of Sr in
928 covariance with Zr and Th (Fix and Fix). The cap dolostone in this study displayed a low
929 Sr content, ranging from 30 to 70 ppm, in contrast to the cap limestones with Sr 300-1400
930 ppm. The interpretation of primary dolomite precipitation by Nogueira et al.2003; 2019,
931 Font et al. 2006; Romero et al. 2020; Soares et al. 2020, and Santos et al. 2021, 2023 is
932 consistent with our data because ancient dolomite commonly has significantly lower Sr
933 concentrations (20–70 ppm) (Baker and Burns, 1985; Vahrenkamp and Swart, 1990).
934 This abrupt transition in Sr concentrations follows a decrease in the Mg/Ca ratio (0.9 to
935 0.0) (see Fig. x). According to Ahm et al. (2019), dolomitization related to an aragonitic
936 primary fabric is consistent with fluid flow and seawater upwelling during global
937 deglaciation. Our data agree with an upwelling event and a syn-deglacial dolomitization
938 event, as previously discussed:

939 1. Mixing of meltwater and seawater (Y/Ho = 27 to 71)
940 2. Shallow seawater interacting with deep water (high Eu/Eu anomalies, suggesting
941 the upwelling of syndepositional T-high hydrothermal fluids)

3. Low correlation between Mg/Ca and $\delta^{13}C$ and $\delta^{18}O$, suggesting that dolomitization occurred at least early diagenesis.
4. The excellent preservation of gypsum pseudomorphs indicates early dolomitization (see Santos et al. 2021, 2023).

Despite our evidence agreeing with upwelling events, our sedimentological data disagree with an abrupt increase in water depth as a controller for the last dolomitization event. Although limestone beds are associated with a moderately deep platform, aragonite crystal fans are truncated, indicating wave action in shallow waters (Soares et al. 2020), and these precipitated on the seafloor were possibly dispersed as micrite by oscillation (Viera et al. 2015). The hydrodynamic conditions were similar during upper cap dolostone and cap limestone precipitation in a shallow platform influenced by wave actions. Despite this evidence, the product of the interaction with the mats still needs to be clarified if we initially have a precipitated proto-dolomite according to the organogenic model (Vasconcelos et al.1994, Dupraz 2009; Qiu et al. 2017; Chang et al. 20) or if it was initially aragonite as suggested by Ahm et al. 2019. The concentration of Mg remained constant during the restriction of paleoenvironmental conditions on dolomitic platforms. The rapid sea-level rise facilitated more excellent dispersion of Mg ions, leading to the definitive interruption of dolomicrite precipitation, abruptly replaced by $CaCO_3$ supersaturated seas with massive aragonite precipitation influenced by a long-lasting transgression, still occurring during the Lower Ediacaran.

7. CONCLUSION

The REE+Y patterns and δ13C values observed in the Puga cap carbonate provide valuable insights into post-snowball Earth paleoceanographic conditions. The low Y/Ho ratios in the cap dolostones suggest dilution of seawater composition due to meltwater

influx from continents (Y/Ho ~29). Conversely, superchondritic Y/Ho ratios up to 71 in the basal cap dolostones suggest upwelling of hypersaline seawater in coastal areas. In addition, the flattened REE+Y pattern with a positive Eu anomaly (up to 3.2) may suggest meltwater with influences from a region with volcanic rocks (e.g., Amazon Craton). REE+Y mass fractions in such settings may not accurately reflect global ocean water composition; instead, they primarily fractionate in response to local factors related to alkalinity and freshwater mixing. These findings imply that ocean destratification is associated with ocean circulation and glacial isostatic adjustment, with reduced siliciclastic inflow supporting a siliciclastic starvation model or rapid precipitation. The recurrence of shallow-water conditions, attributed to early evidence of relative sealevel decline, is linked to local ice sheet recession (ice gravity). This led to the continuous uplift of the coastal zone, the creation of an isolated shelf protected by ocean dynamics, and deformation in diamictite, resulting in irregular substrate relief morphologies. This phase witnessed the flourishing of extensive microbial communities and the rapid recovery of primary productivity, which induced dolomite precipitation in the coastal setting. Mixing water masses and massive detrital input, as indicated by the increase of insoluble elements (e.g., REE, Zr, and Th), generated a geochemical change caused by CaCO3-supersaturated seas influenced by significant landward shoreline migration during the longterm transgression. These observations comprehensively explain the complex interplay between post-glaciation and paleoceanographic dynamics during the Cryogenian-Ediacaran boundary.

References

Alexander, B.W., Bau, M., Andersson, P., Dulski, P., 2008. Continentally derived solutes in shallow Archean seawater: rare earth element and Nd isotope evidence in iron formation from the 2.9 Ga Pongola Supergroup, South Africa. Geochim. Cosmochim. Acta 72 (2), 378394.

Alibo, D.S., Nozaki, Y., 1999. Rare earth elements in seawater: particle association, shale normalization, and Ce oxidation. Geochim. Cosmochim. Acta 63 (34), 363372.

Allen, P.A., Hoffman, P.F., 2005. Extreme winds and waves in the aftermath of a Neoproterozoico glaciation. Nature 433, 123127.

Allwood, A.C., Kamber, B.S., Walter, M.R., Burch, I.W., Kanik, I., 2010. Trace elements record the depositional history of an Early Archean stromatolitic carbonate platform. Chem. Geol. 270 (14), 148163.

Alvarenga, C.J.S., Boggiani, P.C., Babinski, M., Dardenne, M.A., Figueiredo, M.F., Dantas, E.L., Uhlein, A., Santos, R.V., Sial, A.N., Trompette, R., 2011. Glacially influenced sedimentation of the Puga Formation, Cuiaba´ Group, and Jacadigo Group, and associated carbonates of the Araras and Corumba´ groups, Paraguay Belt, Brazil. Geol. Soc. Memoir 36 (1), 487–497.

Asmerom, Y., Jacobsen, S.B., Knoll, A.H., Butterfield, N.J., Swett, K., 1991. Strontium isotopic variations of Neoproterozoic seawater: implications for crustal evolution. Geochim. Cosmochim. Acta 55 (10), 28832894.

Babinski, M., 2011. Geocronologia das glaciaço˜es criogenianas do Brasil Central. Livre Docˆencia. UNIVERSIDADE DE SA˜O PAULO.

Babinski, M., Boggiani, P.C., Trindade, R.I.F.D., Fanning, C.M., 2013. Detrital zircon ages and geochronological constraints on the Neoproterozoic Puga diamictites and associated BIFs in the southern Paraguay Belt, Brazil. Gondwana Res. 23 (3), 988–997.

Babinski, M., Trindade, R.I.F.D., Alvarenga, C.J.S., Boggiani, P.C., Liu, D., Santos, R.V., Brito Neves, B.D., 2006. Chronology of Neoproterozoic ice ages in central Brazil. In South American Symposium on Isotope Geology (Vol. 5, pp. 223226).

Banner, J.L., Hanson, G.N., 1990. Calculation of simultaneous isotopic and trace element variations during waterrock interaction with applications to carbonate diagenesis. Geochim. Cosmochim. Acta 54 (11), 31233137.

Bao, H., Lyons, J.R., Zhou, C., 2008. Triple oxygen isotope evidence for elevated CO2 levels after a Neoproterozoic glaciation. Nature 453 (7194), 504506.

Barrat, J.A., Boulegue, J., Tiercelin, J.J., Lesourd, M., 2000. Strontium isotopes and rareearth element geochemistry of hydrothermal carbonate deposits from Lake Tanganyika, East Africa. Geochim. Cosmochim. Acta 64 (2), 287298.

Barrett, T.J., 1981. Chemistry and mineralogy of Jurassic bedded chert overlying ophiolites in the North Apennines, Italy. Chem. Geol. 34 (34), 289317.

Bau, M., 1991. Rare earth element mobility during hydrothermal and metamorphic fluidrock interaction and the significance of the oxidation state of europium. Chem. Geol. 93 (34), 219230.

Bau, M., Dulski, P., 1996. Distribution of yttrium and rareearth elements in the Penge and Kuruman ironformations, Transvaal Supergroup, South Africa. Precambrian Res. 79 (12), 3755.

Bau, M., Dulski, P., 1999. Comparing yttrium and rare earths in hydrothermal fluids

from the MidAtlantic Ridge: Implications for Y and REE behaviour during nearvent mixing and for the Y/Ho ratio of Proterozoic seawater. Chem. Geol. 155 (12), 7790.
Bau, M., Koschinsky, A., Dulski, P., Hein, J.R., 1996. Comparison of the partitioning behaviours of yttrium, rare earth elements, and titanium between hydrogenetic marine ferromanganese crusts and seawater. Geochim. Cosmochim. Acta 60, 1709–1725.
Benn, D.I., Le Hir, G., Bao, H., Donnadieu, Y., Dumas, C., Fleming, E.J., Fairchild, I.J., 2015. Orbitally forced ice sheet fluctuations during the Marinoan Snowball Earth glaciation. Nat. Geosci. 8 (9), 704707.
Bolhar, R., Kamber, B.S., Moorbath, S., Fedo, C.M., Whitehouse, M.J., 2004. Characterisation of early Archaean chemical sediments by trace element signatures. Earth Planet. Sci. Lett. 222 (1), 4360.
Bolhar, R., Hofmann, A., Siahi, M., Feng, Y.X., Delvigne, C., 2015. A trace element and Pb isotopic investigation into the provenance and deposition of stromatolitic carbonates, ironstones and associated shales of the~ 3.0 Ga Pongola Supergroup, Kaapvaal Craton. Geochim. Cosmochim. Acta 158, 5778.
Bolhar, R., Van Kranendonk, M.J., 2007. A nonmarine depositional setting for the northern Fortescue Group, Pilbara Craton, inferred from trace element geochemistry of stromatolitic carbonates. Precambrian Res. 155 (34), 229250.
Bostro¨m, K., Kraemer, T., Gartner, S., 1973. Provenance and accumulation rates of opaline silica, Al, Ti, Fe, Mn, Cu, Ni and Co in Pacific pelagic sediments. Chemical Geology 11 (2), 123–148.
Brand, U., Veizer, J., 1981. Chemical diagenesis of a multicomponent carbonate system; 2, stable isotopes. J. Sediment. Res. 51 (3), 987997.
Bristow, T.F., Bonifacie, M., Derkowski, A., Eiler, J.M., Grotzinger, J.P., 2011. A hydrothermal origin for isotopically anomalous cap dolostone cements from south China. Nature 474, 68–71.
Carignan, J., Hild, P., Mevelle, G., Morel, J., & Yeghicheyan, D., 2001. Routine analyses of trace elements in geological samples using flow injection and low pressure on-line liquid chromatography coupled to ICP-MS: A study of geochemical reference materials BR, DR-N, UB-N, AN-G and GH. Geostandards Newsletter, 25(2-3), 187- 198.
Carvalho, D.F., Nogueira, A.C., Macambira, M.J., Lana, C.C., Santos, R.F., Gu´elard, J., Sansjofre, P., 2023. Constraining the Diagenesis of the Puga Cap Carbonate from U–Pb In-Situ Dating of Seafloor Crystal Fans, Southern Amazonian Craton. Brazil. Terra Nova, 35(4), 276-284.
Caxito, F.A., Frei, R., Uhlein, G.J., Dias, T.G., A´rting, T.B., Uhlein, A., 2018.Multiproxy geochemical and isotope stratigraphy records of a Neoproterozoic Oxygenation Event in the Ediacaran Sete Lagoas cap carbonate, Bambuí Group, Brazil. Chem. Geol. 481, 119132.
Chen, J., Algeo, T.J., Zhao, L., Chen, Z.Q., Cao, L., Zhang, L., Li, Y., 2015. Diagenetic uptake of rare earth elements by bioapatite, with an example from Lower Triassic conodonts of South China. Earth Sci. Rev. 149, 181202.
Chen, X., Zhou, Y., Shields, G.A., 2022. Progress towards an improved Precambrian seawater 87Sr/86Sr curve. Earth-Science Reviews 224, 103869.
Corsetti, F.A., Lorentz, N.J., 2006. On Neoproterozoic cap carbonates as chronostratigraphic markers. In Neoproterozoic Geobiology and Paleobiology (pp. 273294). Dordrecht: Springer Netherlands.

Creveling, J.R., Mitrovica, J.X., 2014. The sealevel fingerprint of a Snowball Earth deglaciation. Earth Planet. Sci. Lett. 399, 74–85.
Crockford, P.W., Cowie, B.R., Johnston, D.T., Hoffman, P.F., Sugiyama, I., Pellerin, A., Wing, B.A., 2016. Triple oxygen and multiple sulfur isotope constraints on the evolution of the postMarinoan sulfur cycle. Earth Planet. Sci. Lett. 435, 7483.
Crockford, P.W., Hodgskiss, M.S., Uhlein, G.J., Caxito, F., Hayles, J.A., Halverson, G.P., 2018. Linking paleocontinents through triple oxygen isotope anomalies. Geology 46 (2), 179182.
Crockford, P.W., Kunzmann, M., Bekker, A., Hayles, J., Bao, H., Halverson, G.P., et al., 2019. Claypool continued: Extending the isotopic record of sedimentary sulfate. Chemical Geology 513, 200–225.
Crockford, P.W., Kunzmann, M., Bla¨ttler, C.L., KalderonAsael, B., Murphy, J.G., Ahm, A. S., Higgins, J.A., 2021a. Reconstructing Neoproterozoic seawater chemistry from early diagenetic dolomite. Geology 49 (4), 442446.
Crockford, P.W., Mehra, A., Hoffman, P.F., 2021b. An occurrence of radially-symmetric sedimentary structures in the basal Ediacaran cap dolostone (Keilberg Member) of the Otavi Group. Comm. Geol. Surv. Namibia.
Cui, H., Kaufman, A.J., Xiao, S., Zhou, C., Liu, X.M., 2017. Was the Ediacaran Shuram Excursion a globally synchronized early diagenetic event? Insights from methanederived authigenic carbonates in the uppermost Doushantuo Formation, South China. Chem. Geol. 450, 5980.
Cui, H., Kitajima, K., Orland, I.J., Baele, J.-M., Denny, A., Spicuzza, M.J., Fournelle, J.H., Goderis, S., de Winter, N.J., Valley, J.W., 2024. Questioning the role of methane in the wake of a snowball Earth: Insights from isotopically anomalous cap dolostone cements with a complex diagenetic history. Geochim. Cosmochim. Acta 364, 195–210.
Cui, Y., Lang, X., Li, F., Huang, K., Ma, H., Li, C., Shen, B., 2019. Germanium/silica ratio and rare earth element composition of silicafilling in sheet cracks of the Doushantuo cap carbonates, South China: Constraining hydrothermal activity during the Marinoan snowball Earth glaciation. Precambrian Res. 332, 105407.
Deng, Y., Ren, J., Guo, Q., Cao, J., Wang, H., Liu, C., 2017. Rare earth element geochemistry characteristics of seawater and porewater from deep sea in western Pacific. Sci. Rep. 7 (1), 16539.
Derry, L.A., 2010. A burial diagenesis origin for the Ediacaran Shuram–Wonoka carbon isotope anomaly. Earth and Planetary Science Letters 294 (1–2), 152–162.
Derry, L.A., Keto, L.S., Jacobsen, S.B., Knoll, A.H., Swett, K., 1989. Sr isotopic variations in Upper Proterozoic carbonates from Svalbard and East Greenland. Geochim.Cosmochim. Acta 53 (9), 23312339.
Derry, L.A., Kaufman, A.J., Jacobsen, S.B., 1992. Sedimentary cycling and environmental change in the Late Proterozoic: evidence from stable and radiogenic isotopes. Geochim. Cosmochim. Acta 56 (3), 13171329.
Derry, L.A., Brasier, M.D., Corfield, R.E.A., Rozanov, A.Y., Zhuravlev, A.Y., 1994. Sr and C isotopes in Lower Cambrian carbonates from the Siberian craton: a paleoenvironmental record during the ‘Cambrian explosion. Earth and Planetary Science Letters 128 (3–4), 671–681.
Dong, G., Xiong, G., Dan, Y., Dong, J., Li, X., Ma, L., Liu, C., 2023. Sedimentary model of the Ediacaran Doushantuo cap carbonates from the southeastern

margin of the Yangtze Block: Evidence from carbon and oxygen isotopes and elemental geochemistry. Geol. J. 58 (3), 1012–1041.
Douville, E., Bienvenu, P., Charlou, J.L., Donval, J.P., Fouquet, Y., Appriou, P., Gamo, T., 1999. Yttrium and rare earth elements in fluids from various deepsea hydrothermal systems. Geochim. Cosmochim. Acta 63 (5), 627643.
Elderfield, H., Sholkovitz, E.T., 1987. Rare earth elements in the pore waters of reducing nearshore sediments. Earth and Planetary Science Letters 82 (3–4), 280–288.
Fabre, S., Berger, G., 2012. How tillite weathering during the snowball Earth aftermath induced cap carbonate deposition. Geology 40 (11), 1027–1030.
Fabre, S., Berger, G., Chavagnac, V., Besson, P., 2013. Origin of cap carbonates: An experimental approach. Palaeogeogr. Palaeoclimatol. Palaeoecol. 392, 524533.
Fairchild, I.J., Kennedy, M.J., 2007. Neoproterozoic glaciation in the Earth System. J. Geol. Soc. 164 (5), 895921.
Fogret, L., Sansjofre, P., Lalonde, S.V., 2024. Geochemistry of carbonate microbialites through time and space: Insights from the microbialite collection of the Mus´eum National d'Histoire Naturelle (MNHN), France. Chem. Geol., 122239
Fo¨lling, P.G., Frimmel, H.E., 2002. Chemostratigraphic correlation of carbonate successions in the Gariep and Saldania Belts, Namibia and South Africa. Basin Res. 14 (1), 6988.
Font, E., N´ed´elec, A., Trindade, R.I.F.D., Macouin, M., Charri`ere, A., 2006. Chemostratigraphy of the Neoproterozoic Mirassol d'Oeste cap dolostones (Mato Grosso, Brazil): An alternative model for Marinoan cap dolostone formation. Earth Planet. Sci. Lett. 250 (12), 89103.
Font, E., N´ed´elec, A., Trindade, R.I.F.D., Moreau, C., 2010. Fast or slow melting of the Marinoan snowball Earth? The cap dolostone record. Palaeogeogr. Palaeoclimatol. Palaeoecol. 295 (12), 215225.
Frimmel, H.E., 2009. Trace element distribution in Neoproterozoic carbonates as palaeoenvironmental indicator. Chem. Geol. 258 (34), 338353.
Gaia, V.C.S., Nogueira, A.C.R., Domingos, F.H.G., Sansjofre, P., Bandeira, J., Oliveira, J. G.F., Sial, A.N., 2017. The new occurrence of Marinoan cap carbonate in Brazil: the expansion of snowball Earth events to the southwesternmost Amazon Craton. J. South Am. Earth Sci. 76, 446–459.
German, C.R., Elderfield, H., 1989. Rare earth elements in Saanich Inlet, British Columbia, a seasonally anoxic basin. Geochimica et Cosmochimica Acta 53 (10), 2561–2571.
German, C.R., Elderfield, H., 1990. Application of the Ce anomaly as a paleoredox indicator: The ground rules. Paleoceanography 5 (5), 823833.
Gernon, T.M., Hincks, T.K., Tyrrell, T., Rohling, E.J., Palmer, M.R., 2016. Snowball Earth ocean chemistry driven by extensive ridge volcanism during Rodinia breakup. Nat. Geosci. 9 (3), 242248.
Giddings, J.A., Wallace, M.W., 2009. Faciesdependent δ13C variation from a Cryogenian platform margin, South Australia: Evidence for stratified Neoproterozoic oceans? Palaeogeogr. Palaeoclimatol. Palaeoecol. 271 (34), 196214.
Haley, B.A., Klinkhammer, G.P., McManus, J., 2004. Rare earth elements in pore waters of marine sediments. Geochimica et Cosmochimica Acta 68 (6), 1265–

1279.
Halverson, G.P., Dud´as, F.O¨ ., Maloof, A.C., Bowring, S.A., 2007. Evolution of the 87Sr/86Sr composition of Neoproterozoic seawater. Palaeogeogr. Palaeoclimatol. Palaeoecol. 256 (34), 103129.
He, R., Lang, X., Shen, B., 2021. A rapid rise of seawater δ13C during the deglaciation of the Marinoan Snowball Earth. Global Planet. Change 207, 103672.
Higgins, J.A., Bl¨attler, C.L., Lundstrom, E.A., SantiagoRamos, D.P., Akhtar, A.A., Ahm, A.C., Swart, P.K., 2018. Mineralogy, early marine diagenesis, and the chemistry of shallowwater carbonate sediments. Geochim. Cosmochim. Acta 220, 512534.
Higgins, J.A., Schrag, D.P., 2003. Aftermath of a Snowball Earth. Geochem. Geophys.Geosyst. 4 (3).
Hodgskiss, M.S., Lalonde, S.V., Crockford, P.W., Hutchings, A.M., 2021. A carbonate molybdenum isotope and cerium anomaly record across the endGOE: Local records of global oxygenation. Geochim. Cosmochim. Acta 313, 313339.
Hoffman, P.F., Scharg, D.P., 2002. The Snowball Earth hypothesis: testing the limits of global changes. Terra Nova 14, 129155.
Hoffman, P.F., Kaufman, A.J., Halverson, G.P., Schrag, D.P., 1998. A Neoproterozoic snowball earth. Science 281 (5381), 13421346.
Hoffman, P.F., Abbot, D.S., Ashkenazy, Y., Benn, D.I., Brocks, J.J., Cohen, P.A., Warren, S.G., 2017. Snowball Earth climate dynamics and Cryogenian geobiology. Sci. Adv. 3 (11), e1600983.
Hoffman, P.F., Halverson, G.P., Schrag, D.P., Higgins, J.A., Domack, E.W., Macdonald, F. A., Nelson, L.L., 2021. Snowballs in Africa: sectioning a longlived Neoproterozoic carbonate platform and its bathyal foreslope (NW Namibia). Earth Sci. Rev. 219, 103616.
Hohl, S.V., Becker, H., Gamper, A., Jiang, S.Y., Wiechert, U., Yang, J.H., Wei, H.Z., 2015a. Secular changes of water chemistry in shallowwater Ediacaran Ocean: Evidence from carbonates at Xiaofenghe, Three Gorges area, Yangtze Platform, South China. Precambrian Res 270, 5079.
Hohl, S.V., Becker, H., Herzlieb, S., Guo, Q., 2015b. Multiproxy constraints on alteration and primary compositions of Ediacaran deepwater carbonate rocks, Yangtze Platform, South China. Geochim. Cosmochim. Acta 163, 262278.
Hohl, S.V., Becker, H., Jiang, S.Y., Ling, H.F., Guo, Q., Struck, U., 2017. Geochemistry of Ediacaran cap dolostones across the Yangtze Platform, South China: Implications for diagenetic modification and seawater chemistry in the aftermath of the Marinoan glaciation. J. Geol. Soc. 174 (5), 893912.
Hohl, S.V., Rodler, A.S., Viehmann, S., Huang, X., Xu, J., Gaucher, C., Frei, R., 2022. C, Sr, Nd isotope chemostratigraphy and zircon provenance of the Witvlei Group (Namibia): Neoproterozoic glaciations and seawater evolution. Precambrian Res. 372, 106600.
Huang, J., Chu, X., Chang, H., Feng, L., 2009. Trace element and rare earth element of cap carbonate in Ediacaran Doushantuo Formation in Yangtze Gorges. Chin. Sci. Bull. 54 (18), 32953302.
Huang, J., Chu, X., Jiang, G., Feng, L., Chang, H., 2011. Hydrothermal origin of elevated iron, manganese and redoxsensitive trace elements in the c. 635 Ma Doushantuo cap carbonate. J. Geol. Soc. 168 (3), 805816.
Hurtgen, M.T., Halverson, G.P., Arthur, M.A., Hoffman, P.F., 2006. Sulfur cycling

in the aftermath of a 635Ma snowball glaciation: Evidence for a synglacial sulfidic deep ocean. Earth Planet. Sci. Lett. 245 (34), 551570.
Jacobsen, S.B., Kaufman, A.J., 1999. The Sr, C and O isotopic evolution of Neoproterozoic seawater. Chem. Geol. 161 (13), 3757.
Jiang, G., Kennedy, M.J., ChristieBlick, N., 2003. Stable isotopic evidence for methane seeps in Neoproterozoic postglacial cap carbonates. Nature 426 (6968), 822826.
Jiang, G., Kennedy, M.J., Christie-Blick, N., Wu, H., Zhang, S., 2006. Stratigraphy, sedimentary structures, and textures of the late Neoproterozoic Doushantuo cap carbonate in South China. Journal of Sedimentary Research 76 (7), 978–995.
Jiang, S.Y., Zhao, H.X., Chen, Y.Q., Yang, T., Yang, J.H., Ling, H.F., 2007. Trace and rare earth element geochemistry of phosphate nodules from the lower Cambrian black shale sequence in the Mufu Mountain of Nanjing, Jiangsu province, China. Chem. Geol. 244 (34), 584604.
Kamber, B.S., Webb, G.E., 2001. The geochemistry of late Archaean microbial carbonate: Implications for ocean chemistry and continental erosion history. Geochim. Cosmochim. Acta 65, 2509–2525.
Kamber, B.S., Greig, A., Collerson, K.D., 2005. A new estimate for the composition of weathered young upper continental crust from alluvial sediments, Queensland, Australia. Geochimica et Cosmochimica Acta 69 (4), 1041–1058.
Kaufman, A.J., Jacobsen, S.B., Knoll, A.H., 1993. The Vendian record of Sr and C isotopic variations in seawater: implications for tectonics and paleoclimate. Earth Planet. Sci. Lett. 120 (3–4), 409–430.
Kaufman, A.J., Knoll, A.H., 1995. Neoproterozoic variations in the C-isotopic composition of seawater: Stratigraphic and biogeochemical implications. Precambrian Res. 73 (1–4), 27–49.
Kennedy, M., Mrofka, D., Von Der Borch, C., 2008. Snowball Earth termination by destabilization of equatorial permafrost methane clathrate. Nature 453 (7195), 642–645.
Kim, J.H., Lee, B.O., Lee, C.B., Jee, S.H., Yoon, Y.S., 2012. Formation of intermetallic compound at interface between rare earth elements and ferritic-martensitic steel by fuel cladding chemical interaction. Journal of Rare Earths 30 (6), 599–603.
Kirschvink, J.L., 1992. Late Proterozoic low-latitude global glaciation: The snowball Earth.
Klein, C., Beukes, N.J., 1993. Sedimentology and geochemistry of the glaciogenic late Proterozoic Rapitan iron-formation in Canada. Economic Geology 88 (3), 542–565.
Klinkhammer, G.P., Elderfield, H., Edmond, J.M., Mitra, A., 1994a. Geochemical implications of rare earth element patterns in hydrothermal fluids from mid-ocean ridges. Geochim. Cosmochim. Acta, 58(23), 5105-5113.
Klinkhammer, G., German, C.R., Elderfield, H., Greaves, M., Mitra, A., 1994b. Rare earth elements in hydrothermal fluids and plume particulates by inductively coupled plasma mass spectrometry. Mar. Chem., 45(3), 179-186.
Langarica, Y.R., S´anchez-Beristain, F., Simon, K., 2020. REE+ Y patterns and positive europium anomalies recorded in limestones from zone XX of the Tlayúa Quarry Konservat-Lagerst¨atte (Tlayúa Formation, Lower Cretaceous; Tepexi de Rodríguez, Mexico). Arabian J. Geosci. 13 (20), 1076.
Lawrence, M.G., Kamber, B.S., 2006. The behaviour of the rare earth elements

during estuarine mixing—revisited. Mar. Chem. 100 (1–2), 147–161.
Lawrence, M.G., Greig, A., Collerson, K.D., Kamber, B.S., 2006. Rare earth element and yttrium variability in South East Queensland waterways. Aquat. Geochem. 12, 39–72.
Li, D., Pierrehumbert, R.T., 2011. Sea glacier flow and dust transport on Snowball Earth. Geophys. Res. Lett. 38 (17).
Li, F., Webb, G.E., Algeo, T.J., Kershaw, S., Lu, C., Oehlert, A.M., et al., 2019. Modern carbonate ooids preserve ambient aqueous REE signatures. Chemical Geology 509, 163–177.
Ling, H.F., Chen, X., Li, D.A., Wang, D., Shields-Zhou, G.A., Zhu, M., 2013. Cerium anomaly variations in Ediacaran–earliest Cambrian carbonates from the Yangtze Gorges area, South China: implications for oxygenation of coeval shallow seawater. Precambr. Res. 225, 110–127.
Liu, Y., & Peltier, W.R., 2010. A carbon cycle coupled climate model of Neoproterozoic glaciation: Influence of continental configuration on the formation of a "soft snowball". Journal of Geophysical Research: Atmospheres, 115(D17).
Liu, X.M., Hardisty, D.S., Lyons, T.W., Swart, P.K., 2019. Evaluating the fidelity of the cerium paleoredox tracer during variable carbonate diagenesis on the Great Bahamas Bank. Geochim. Cosmochim. Acta 248, 25–42.
Liu, C., Wang, Z., Raub, T.D., Macdonald, F.A., Evans, D.A., 2014. Neoproterozoic cap- dolostone deposition in stratified glacial meltwater plume. Earth Planet. Sci. Lett. 404, 22–32.
Liu, C., Wang, Z., Macdonald, F.A., 2018. Sr and Mg isotope geochemistry of the basal Ediacaran cap limestone sequence of Mongolia: Implications for carbonate diagenesis, mixing of glacial meltwaters, and seawater chemistry in the aftermath of Snowball Earth. Chem. Geol. 491, 1–13.
Lu, F.H., Meyers, W.J., 1998. Massive dolomitization of a late Miocene carbonate platform: A case of mixed evaporative brines with meteoric water, Nijar, Spain. Sedimentology 45 (2), 263–277.
Marchig, V., Gundlach, H., Mo¨ller, P., Schley, F., 1982. Some geochemical indicators for discrimination between diagenetic and hydrothermal metalliferous sediments. Mar. Geol. 50 (3), 241–256.
McArthur, J.M., 1994. Recent trends in strontium isotope stratigraphy. Terra Nova 6 (4), 331–358.
McGee, B., Babinski, M., Trindade, R., Collins, A.S., 2018. Tracing final Gondwana assembly: Age and provenance of key stratigraphic units in the southern Paraguay Belt, Brazil. Precambr. Res. 307, 1–33.
McLennan, S.M., 1989. Rare earth elements in sedimentary rocks: Influence of provenance and sedimentary processes. In: Lipin, B.R., McKay, G.A. (Eds.), Geochemistry and Mineralogy of Rare Earth Elements. De Gruyter, Berlin, pp. 169–200.
McLennan, S.M., Bock, B., Hemming, S.R., Horowitz, J.A., Lev, S.M., McDaniel, D.K., 2003. The roles of provenance and sedimentary processes in the geochemistry of sedimentary rocks. Geochem. Sediment. Rocks 4, 7–38.
Melezhik, V.A., Gorokhov, I.M., Fallick, A.E., Gjelle, S., 2001. Strontium and carbon isotope geochemistry applied to dating of carbonate sedimentation: An example from high-grade rocks of the Norwegian Caledonides. Precambrian Res. 108 (3–4), 267–292.

Meyer, E.E., Quicksall, A.N., Landis, J.D., Link, P.K., Bostick, B.C., 2012. Trace and rare earth elemental investigation of a Sturtian cap carbonate, Pocatello, Idaho: evidence for ocean redox conditions before and during carbonate deposition. Precambrian Res. 192, 89–106.

Milhomem, J.M.N., Nogueira, A.C.R., Macambira, M.J.B., 2013. A seç˜ao-tipo da Formaça˜o Serra do Quilombo, Grupo Araras, Neoproterozoico da Faixa Paraguai Norte, Mato Grosso. Braz. J. Geol. 43, 385–400.

Mitchell, R.N., Gernon, T.M., Cox, G.M., Nordsvan, A.R., Kirscher, U., Xuan, C., He, X., 2021. Orbital forcing of ice sheets during snowball Earth. Nat. Commun. 12 (1), 4187.

N´ed´elec, A., Affaton, P., France-Lanord, C., Charri`ere, A., Alvaro, J., 2007. Sedimentology and chemostratigraphy of the Bwipe Neoproterozoic cap dolostones (Ghana, Volta Basin): A record of microbial activity in a peritidal environment. CR Geoscience 339 (3–4), 223–239.

Nogueira, A.C.R., Riccomini, C., 2006. O Grupo Araras (Neoproterozoico) na parte norte da Faixa Paraguai e Sul do Cra´ton Amazoˆnico. Rev. Bras. Geociˆencias 36, 576–587.

Nogueira, A.C.R., Riccomini, C., Sial, A.N., Moura, C.A.V., Fairchild, T.R., 2003. Softsediment deformation at the base of the neoproterozoic Puga cap carbonate (southwestern Amazon Craton, Brazil): confirmation of rapid icehouse to greenhouse transition in snowball Earth. Geology 31 (7), 613–616.

Nogueira, A.C.R., Riccomini, C., Sial, A.N., Moura, C.A.V., Trindade, R.I.F., Fairchild, T. R., 2007. Carbon and strontium isotope fluctuations and paleoceanographic changes in the late neoproterozoic Araras carbonate platform, southern Amazon Craton, Brazil. Chem. Geol. 237 (1), 168–190.

Nogueira, A.C.R., Romero, G.R., Mecenero, E.A., Sanchez, F.H.G.D., Bandeira, J., Dos Santos, I.M., Pinheiro, R.V.L., Soares, J.L., Lafon, J.M., Afonso, J.W.L., Santos, H.P., Rudnitzki, I.D., 2019. The cryogenian-ediacaran boundary in the southern Amazon Craton. In: Sial, A.N., Gaucher, C., Ramkumar, M., Ferreira, V.P. (Eds.), Chemostratigraphy across Major Chronological Boundaries. Willey, New York, pp. 89–114.

Nogueira, A.C.R., Santos, R.F., Romero, G.R., Bandeira, J., Riccomini, C., Barrera, I.A.R., Silva, P.A.S., Soares, J.L., Fairchild, T., Nogueira, A.A.E., Goes, A.M., Oliveira, R.S., Medeiros, R.S.P., Andrade, L.S., Brito, A.S., Oliveira, P.G.A., Sodre, A.A.N., Carvalho, D.F., Truckenbrodt, W., 2022. Ediacaran-Cambrian microbialites of the Southern Amazon Craton: relation with the metazoan rise, sea-level changes, and global tectonics, Brazil. J. Geol. 52, e20210065.

Nordsvan, A.R., Barham, M., Cox, G., Kirscher, U., Mitchell, R.N., 2019. Major shoreline retreat and sediment starvation following Snowball Earth. Terra Nova 31 (6), 495–502.

Nothdurft, L.D., Webb, G.E., Kamber, B.S., 2004. Rare earth element geochemistry of late Devonian reefal carbonates, Canning Basin, Western Australia: confirmation of a seawater REE proxy in ancient limestones. Geochim. Cosmochim. Acta 68, 263–283.

Nozaki, Y., 2001. Rare earth elements and their isotopes in the ocean. Encyclopedia Ocean Sci. 4, 2354–2366.

Nozaki, Y., Alibo, D.S., 2003. Importance of vertical geochemical processes in controlling the oceanic profiles of dissolved rare earth elements in the northeastern Indian Ocean. Earth Planet. Sci. Lett. 205 (3–4), 155–172.

Nozaki, Y., Zhang, J., Amakawa, H., 1997. The fractionation between Y and Ho in the marine environment. Earth Planet. Sci. Lett. 148 (1–2), 329–340.
Okubo, J., Muscente, A.D., Luvizotto, G.L., Uhlein, G.J., Warren, L.V., 2018. Phosphogenesis, aragonite fan formation and seafloor environments following the Marinoan glaciation. Precamb. Res. 311, 24–36.
Parsapoor, A., Khalili, M., Mackizadeh, M.A., 2009. The behaviour of trace and rare earth elements (REE) during hydrothermal alteration in the Rangan area (Central Iran).
J. Asian Earth Sci. 34 (2), 123–134.
Peng, Y., Bao, H., Jiang, G., Crockford, P., Feng, D., Xiao, S., Wang, J., 2022. A transient peak in marine sulfate after the 635-Ma snowball Earth. Proc. Natl. Acad. Sci. 119 (19), e2117341119.
Rahlf, P., Laukert, G., Hathorne, E.C., Vieira, L.H., Frank, M., 2021. Dissolved neodymium and hafnium isotopes and rare earth elements in the Congo River Plume: Tracing and quantifying continental inputs into the southeast Atlantic. Geochim. Cosmochim. Acta 294, 192–214.
Ramme, L., Marotzke, J., 2022. Climate and ocean circulation in the aftermath of a Marinoan snowball Earth. Clim. Past 18 (4), 759–774.
Ren, M., Li, R., 2023. Rare earth element signatures of Doushantuo cap dolostones capture an increase in oxygen in the anoxic Ediacaran ocean. Sed. Geol. 446, 106343.
Rodler, A.S., Hohl, S.V., Guo, Q., Frei, R., 2016. Chromium isotope stratigraphy of Ediacaran cap dolostones, Doushantuo formation, South China. Chem. Geol. 436, 24–34.
Romero, J.A.S., Lafon, J.M., Nogueira, A.C.R., Soares, J.L., 2013. Sr isotope geochemistry and Pb-Pb geochronology of the Neoproterozoic cap carbonates, Tangara´ da Serra, Brazil. Int. Geol. Rev. 55 (2), 185–203.
Romero, G.R., Sanchez, E.A.M., Soares, J.L., Nogueira, A.C.R., Fairchild, T.R., 2020. Waxing and waning of microbial laminites in the aftermath of the Marinoan glaciation at the margin of the Amazon Craton (Brazil). Precambrian Res. 348, 105856.
Romero, G.R., Santos, R.F., Nogueira, A.C.R., Rudnitzki, I.D., Fairchild, T.R., 2022. Peritidal microbialites in the upper Araras Group: Morphotypes, potential preservation and the relation with the Ediacaran-Cambrian unconformity in the Araras-Alto Paraguai Basin, southern Amazon Craton. J. S. Am. Earth Sci. 120, 104085.
Rongemaille, E., Bayon, G., Pierre, C., Bollinger, C., Chu, N.C., Fouquet, Y., et al., 2011. Rare earth elements in cold seep carbonates from the Niger delta. Chemical Geology 286 (3–4), 196–206.
Rooney, A.D., Strauss, J.V., Brandon, A.D., Macdonald, F.A., 2015. A Cryogenian chronology: Two long-lasting synchronous Neoproterozoic glaciations. Geology 43 (5), 459–462.
Rudnitzki, I.D., Romero, G.R., Hidalgo, R., Nogueira, A.C.R., 2016. High-frequency peritidal cycles of the upper Araras group: implications for disappearance of the Neoproterozoic carbonate platform in southern Amazon Craton. J. S. Am. Earth Sci. 65, 67–78.
Sansjofre, P., Ader, M., Trindade, R.I.F.D., Elie, M., Lyons, J., Cartigny, P., Nogueira, A.C. R., 2011. A carbon isotope challenge to the snowball Earth. Nat. 478 (7367), 93–96.

Sansjofre, P., Trindade, R.I., Ader, M., Soares, J.L., Nogueira, A.C., Tribovillard, N., 2014. Paleoenvironmental reconstruction of the Ediacaran Araras platform (Western Brazil) from the sedimentary and trace metals record. Precamb. Res. 241, 185–202.

Santos, R.F., Nogueira, A.C.R., Romero, G.R., Soares, J.L., Junior, J.B., 2021. Life in the aftermath of Marinoan glaciation: The giant stromatolite evolution in the Puga cap carbonate, southern Amazon Craton, Brazil. Precamb. Res. 354, 106059.

Santos, R.F., Nogueira, A.C., da Costa, J.B., Sepeda, L.F., Okubo, J., Barros, I.S., Sansjofre, P., 2023. Diagenesis of the Marinoan cap dolostone, Southern Amazon Craton: An unconventional petroleum system in the evolution of the Araras-Alto Paraguai Basin. Mar. Pet. Geol. 158, 106496.

Santos, I.M., Pinheiro, R.V.L., Holdsworth, R.E., Nogueira, A.C.R., Santos, H.P., Domingos, F.H.G., 2020. Basement–cover relationships and deformation in the northern Paraguai belt, Central Brazil: implications for the neoproterozoic-early paleozoic history of western gondwana. J. Geol. Soc. 177 (3), 475–491.

Scherer, M., Seitz, H., 1980. Rare-earth element distribution in Holocene and Pleistocene corals and their distribution during diagenesis. Chem. Geol. 28, 279–289.

Schrag, D.P., Hoffman, P.F., 2001. Life, geology and snowball Earth. Nature 409 (6818), 306.

Sepeda, L.F., Nogueira, A.C.R., dos Santos, R.F., Okubo, J., Silva, P.A.S., Marques, J.C., et al., 2024. Diagenetic and hydrothermal events revealed by an Ediacaran dolomite breccia from the Araras-Alto Paraguai Basin, Southern Amazon Craton. Marine and Petroleum Geology, 107089.

Shen, Y., Zhang, T., Chu, X., 2005. C-isotopic stratification in a Neoproterozoic postglacial ocean. Precambrian Res. 137 (3–4), 243–251.

Shields, G.A., 2005. Neoproterozoic cap carbonates: A critical appraisal of existing models and the plumeworld hypothesis. Terra Nova 17 (4), 299–310.

Shields, G., Stille, P., 2001. Diagenetic constraints on the use of cerium anomalies as palaeoseawater redox proxies: An isotopic and REE study of Cambrian phosphorites. Chem. Geol. 175 (1–2), 29–48.

Shields, G.A., Webb, G.E., 2004. Has the REE composition of seawater changed over geological time?.

Sholkovitz, E.R., 1995. The aquatic chemistry of rare earth elements in rivers and estuaries. Aquat. Geochem. 1, 1–34.

Sholkovitz, E.R., Piepgras, D.J., Jacobsen, S.B., 1989. The pore water chemistry of rare earth elements in Buzzards Bay sediments. Geochim. Cosmochim. Acta 53 (11), 2847–2856.

Soares, J.L., Nogueira, A.C.R., dos Santos, R.F., Sansjofre, P., Ader, M., Truckenbrodt, W., 2020. Microfacies, diagenesis, and hydrocarbon potential of the Neoproterozoic cap carbonate of the southern Amazon Craton. Sediment. Geol. 406, 105720.

Souza, N.M.D.C., Lafon, J.M., Milhomem, J.M., Soares, J.L., 2024. Continental contribution to the marinoan cap carbonate of Tangara´ da Serra–MT, Brazil: further evidence from Sr-Nd-Pb isotope geochemistry. Brazilian Journal of Geology 54 (1), e20230015.

Spence, G.H., Le Heron, D.P., Fairchild, I.J., 2016. Sedimentological perspectives on climatic, atmospheric and environmental change in the Neoproterozoic Era. Sedimentology 63 (2), 253–306.

Tanaka, K., Kawabe, I., 2006. REE abundances in ancient seawater inferred from marine limestone and experimental REE partition coefficients between calcite and aqueous solution. Geochem. J. 40 (5), 425–435.

Taylor, S.R., & McLennan, S.M., 1985. The continental crust: its composition and evolution.

Tepe, N., Bau, M., 2016. Behavior of rare earth elements and yttrium during simulation of Arctic estuarine mixing between glacial-fed river waters and seawater and the impact of inorganic (nano-) particles. Chem. Geol. 438, 134–145.

Trindade, R.I.F.D., Font, E., D'Agrella-Filho, M.S., Nogueira, A.C.R., Riccomini, C., 2003. Low-latitude and multiple geomagnetic reversals in the Neoproterozoic Puga cap carbonate, Amazon Craton. Terra Nova 15 (6), 441–446.

Tziperman, E., Abbot, D.S., Ashkenazy, Y., Gildor, H., Pollard, D., Schoof, C.G., Schrag, D.P., 2012. Continental constriction and oceanic ice-cover thickness in a Snowball-Earth scenario. J. Geophys. Res. Oceans 117 (C5).

Uhlein, G.J., Caxito, F.A., Frei, R., Uhlein, A., Sial, A.N., Dantas, E.L., 2021. Microbially induced chromium isotope fractionation and trace elements behavior in lower Cambrian microbialites from the Jaíba Member, Bambuí Basin, Brazil. Geobiology 19 (2), 125–146.

Verdel, C., Phelps, B., Welsh, K., 2018. Rare earth element and 87Sr/86Sr step-leaching geochemistry of central Australian Neoproterozoic carbonate. Precamb. Res. 310, 229–242.

Vieira, L.C., N´ed´elec, A., Fabre, S., Trindade, R.I., De Almeida, R.P., 2015. Aragonite crystal fans in Neoproterozoic cap carbonates: a case study from Brazil and implications for the post–snowball earth coastal environment. J. Sediment. Res. 85 (3), 285–300.

Wallace, M.W., vS Hood, A., Fayle, J., Hordern, E.S., O'Hare, T.F., 2019. Neoproterozoic marine dolomite hardgrounds and their relationship to cap dolomites. Precamb. Res., 328, 269-286.

Wang, L., Hu, W., Wang, X., Cao, J., Chen, Q., 2014. Seawater normalized REE patterns of dolomites in Geshan and Panlongdong sections, China: Implications for tracing dolomitization and diagenetic fluids. Mar. Petrol. Geol. 56, 63–73.

Wang, J., Jiang, G., Xiao, S., Li, Q., Wei, Q., 2008. Carbon isotope evidence for widespread methane seeps in the ca. 635 Ma Doushantuo cap carbonate in south China. Geology 36 (5), 347–350.

Webb, G.E., Kamber, B.S., 2000. Rare earth elements in Holocene reefal microbialites: A new shallow seawater proxy. Geochim. Cosmochim. Acta 64, 1557–1565.

Wei, G. Y., vS Hood, A., Chen, X., Li, D., Wei, W., Wen, B., et al., 2019. Ca and Sr isotope constraints on the formation of the Marinoan cap dolostones. Earth Planet. Sci. Lett., 511, 202-212.

Wood, S.A., 1990. The aqueous geochemistry of the rare-earth elements and yttrium: 1. Review of available low-temperature data for inorganic complexes and the inorganic REE speciation of natural waters. Chem. Geol. 82, 159–186.

Wu, H.P., Jiang, S.Y., Palmer, M.R., Wei, H.Z., Yang, J.H., 2019. Positive cerium anomaly in the Doushantuo cap carbonates from the Yangtze platform, South China: Implications for intermediate water column manganous conditions in the aftermath of the Marinoan glaciation. Precamb. Res. 320, 93–110.

Wu, J., Liu, Y., Zhao, Z., 2021. How should snowball Earth deglaciation start. J. Geophys. Res. Atmos. 126 (2), e2020JD033833.
Yang, J., Jansen, M.F., Macdonald, F.A., Abbot, D.S., 2017. Persistence of a freshwater surface ocean after a snowball Earth. Geology 45 (7), 615–618.
Yoshioka, H., Asahara, Y., Tojo, B., Kawakami, S.I., 2003. Systematic variations in C, O, and Sr isotopes and elemental concentrations in Neoproterozoic carbonates in Namibia: implications for a glacial to interglacial transition. Precamb. Res. 124 (1), 69–85.
Yu, W., Algeo, T.J., Zhou, Q., Du, Y., Wang, P., 2020. Cryogenian cap carbonate models: A review and critical assessment. Palaeogeogr. Palaeocl., Palaeoecol. 552, 109727.
Zhang, J., Nozaki, Y., 1996. Rare earth elements and yttrium in seawater: ICP-MS determinations in the East Caroline, Coral Sea, and South Fiji basins of the western South Pacific Ocean. Geochim. Cosmochim. Acta 60 (23), 4631–4644.
Zhang, S., Evans, D.A., Li, H., Wu, H., Jiang, G., Dong, J., et al., 2013. Paleomagnetism of the late Cryogenian Nantuo Formation and paleogeographic implications for the South China Block. Journal of Asian Earth Sciences 72, 164–177.
Zhang, K., Zhu, X.K., Yan, B., 2015. A refined dissolution method for rare earth element studies of bulk carbonate rocks. Chem. Geol. 412, 82–91.
Zhao, M., Planavsky, N., Oehlert, A.M., Wei, G., Gong, Z., 2020. Simulating meteoric and mixing zone carbonate diagenesis with a two-dimensional reactive transport model. Am. J. Sci. 320 (7), 599–636.
Zhao, Z., Shen, B., Zhu, J.M., Lang, X., Wu, G., Tan, D., Ma, H., 2021. Active methanogenesis during the melting of Marinoan snowball Earth. Nat. Commun. 12 (1), 955.
Zhao, Y., Wei, W., Santosh, M., Hu, J., Wei, H., Yang, J., Li, S., 2022. A review of retrieving pristine rare earth element signatures from carbonates. Palaeogeogr. Palaeocl., Palaeoecol. 586, 110765.
Zhao, M.Y., Zheng, Y.F., 2014. Marine carbonate records of terrigenous input into Paleotethyan seawater: Geochemical constraints from Carboniferous limestones. Geochim. Cosmochim. Acta 141, 508–531.
Zhao, M.Y., Zheng, Y.F., 2017. A geochemical framework for retrieving the linked depositional and diagenetic histories of marine carbonates. Earth Planet. Sci. Lett. 460, 213–221.
Zhao, Y.Y., Zheng, Y.F., Chen, F., 2009. Trace element and strontium isotope constraints on sedimentary environment of Ediacaran carbonates in southern Anhui, South China. Chemical Geology 265 (3–4), 345–362.
Zhou, G., Luo, T., Zhou, M., Xing, L., Gan, T., 2017. A ubiquitous hydrothermal episode recorded in the sheet-crack cements of a Marinoan cap dolostone of South China: implication for the origin of the extremely 13C-depleted calcite cement. J. Asian Earth Sci. 134, 63–71.

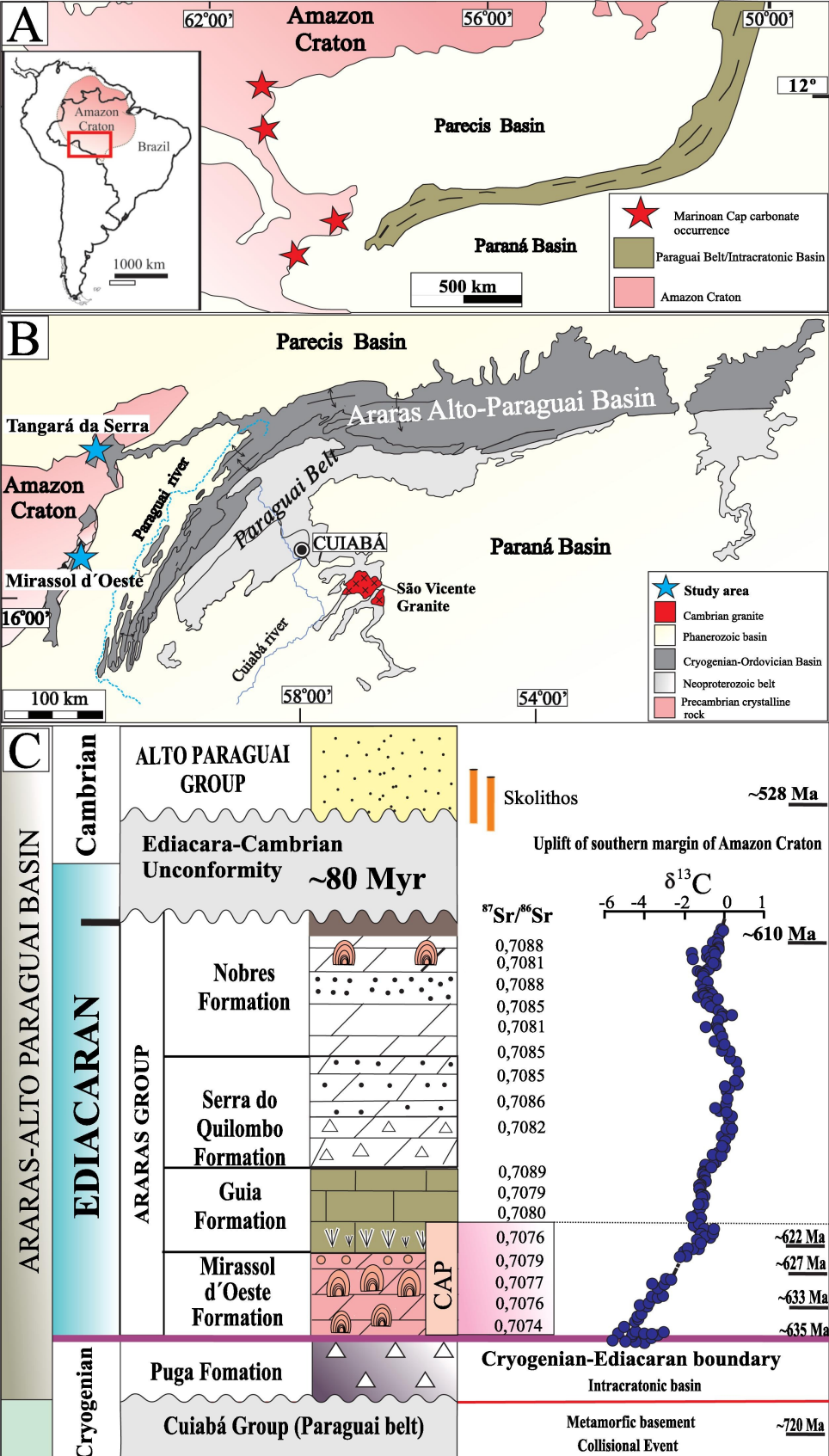
A
62°00'
Amazon Craton
56°00'
50°00'
12°
Amazon Craton
Brazil
1000 km
Parecis Basin
Paraná Basin
500 km
Marinoan Cap carbonate occurrence
Paraguai Belt/Intracratonic Basin
Amazon Craton
B
Parecis Basin
Araras Alto-Paraguai Basin
Tangará da Serra
Amazon Craton
Paraguai river
Paraguai Belt
CUIABÁ
Paraná Basin
Mirassol d´Oeste
São Vicente Granite
16°00'
Cuiabá river
100 km
58°00'
54°00'
Study area
Cambrian granite
Phanerozoic basin
Cryogenian-Ordovician Basin
Neoproterozoic belt
Precambrian crystalline rock
C
ARARAS-ALTO PARAGUAI BASIN
Cambrian
EDIACARAN
Cryogenian
ALTO PARAGUAI GROUP
Skolithos
~528 Ma
Ediacara-Cambrian Unconformity
~80 Myr
Uplift of southern margin of Amazon Craton
ARARAS GROUP
Nobres Formation
Serra do Quilombo Formation
Guia Formation
Mirassol d´Oeste Formation
CAP
δ13C
-6 -4 -2 0 1
87Sr/86Sr
~610 Ma
0,7088
0,7081
0,7088
0,7085
0,7081
0,7085
0,7085
0,7086
0,7082
0,7089
0,7079
0,7080
0,7076
0,7079
0,7077
0,7076
0,7074
~622 Ma
~627 Ma
~633 Ma
~635 Ma
Puga Fomation
Cryogenian-Ediacaran boundary
Intracratonic basin
Cuiabá Group (Paraguai belt)
Metamorfic basement
Collisional Event
~720 Ma

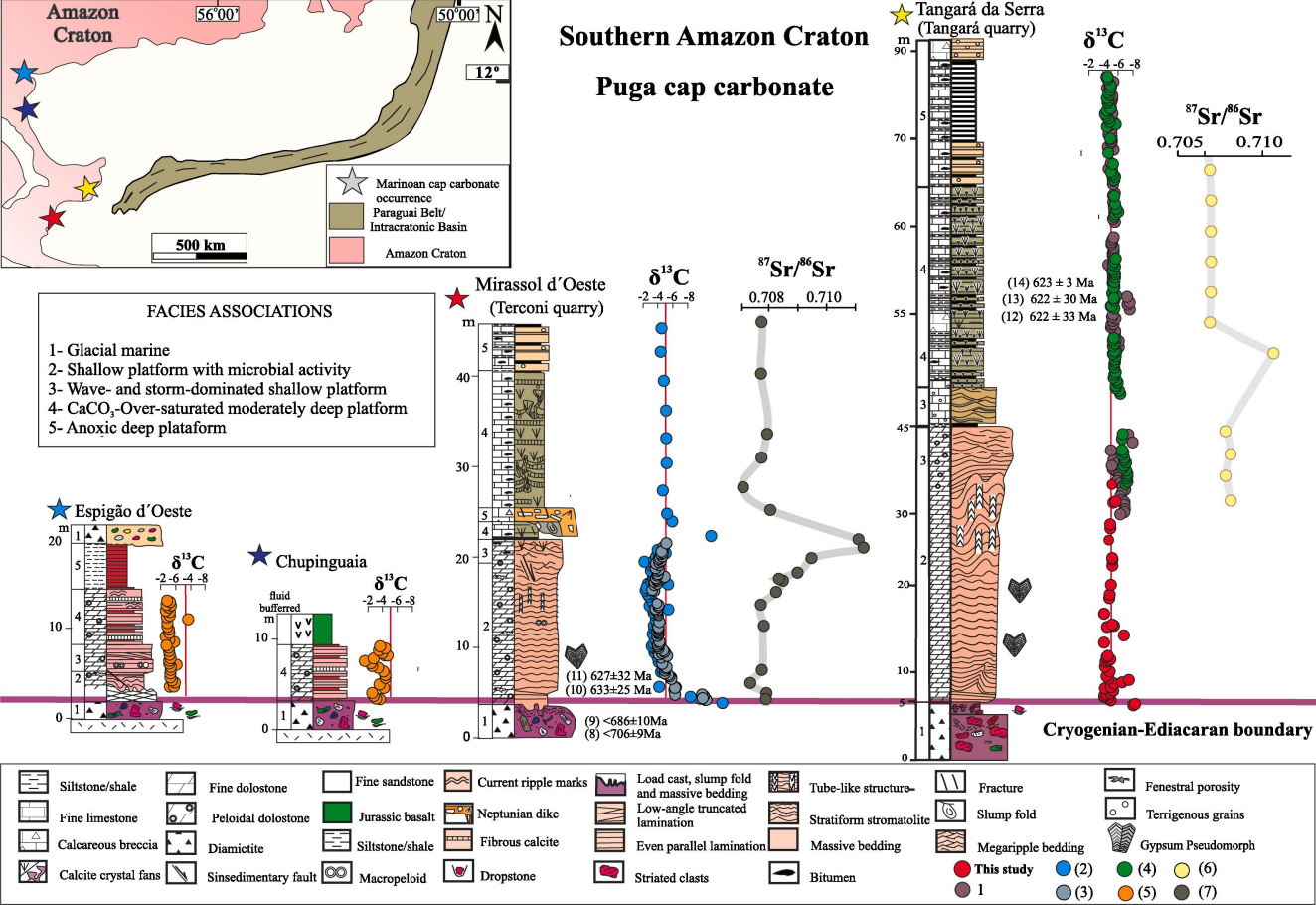
Amazon Craton
56°00'
50°00'
N
12°
Marinoan cap carbonate occurrence
Paraguai Belt/ Intracratonic Basin
Amazon Craton
500 km
Southern Amazon Craton
Puga cap carbonate
FACIES ASSOCIATIONS
1- Glacial marine
2- Shallow platform with microbial activity
3- Wave- and storm-dominated shallow platform
4- $CaCO_3$-Over-saturated moderately deep platform
5- Anoxic deep plataform
Espigão d´Oeste
Chupinguaia
fluid bufferred
Mirassol d´Oeste
(Terconi quarry)
Tangará da Serra
(Tangará quarry)
δ13C
87Sr/86Sr
0.705
0.710
0.708
(14) 623 ± 3 Ma
(13) 622 ± 30 Ma
(12) 622 ± 33 Ma
(11) 627±32 Ma
(10) 633±25 Ma
(9) <686±10Ma
(8) <706±9Ma
Cryogenian-Ediacaran boundary
Siltstone/shale
Fine limestone
Calcareous breccia
Calcite crystal fans
Fine dolostone
Peloidal dolostone
Diamictite
Sinsedimentary fault
Fine sandstone
Jurassic basalt
Siltstone/shale
Macropeloid
Current ripple marks
Neptunian dike
Fibrous calcite
Dropstone
Load cast, slump fold and massive bedding
Low-angle truncated lamination
Even parallel lamination
Striated clasts
Tube-like structure
Stratiform stromatolite
Massive bedding
Bitumen
Fracture
Slump fold
Megaripple bedding
Fenestral porosity
Terrigenous grains
Gypsum Pseudomorph
This study
1
(2)
(3)
(4)
(5)
(6)
(7)

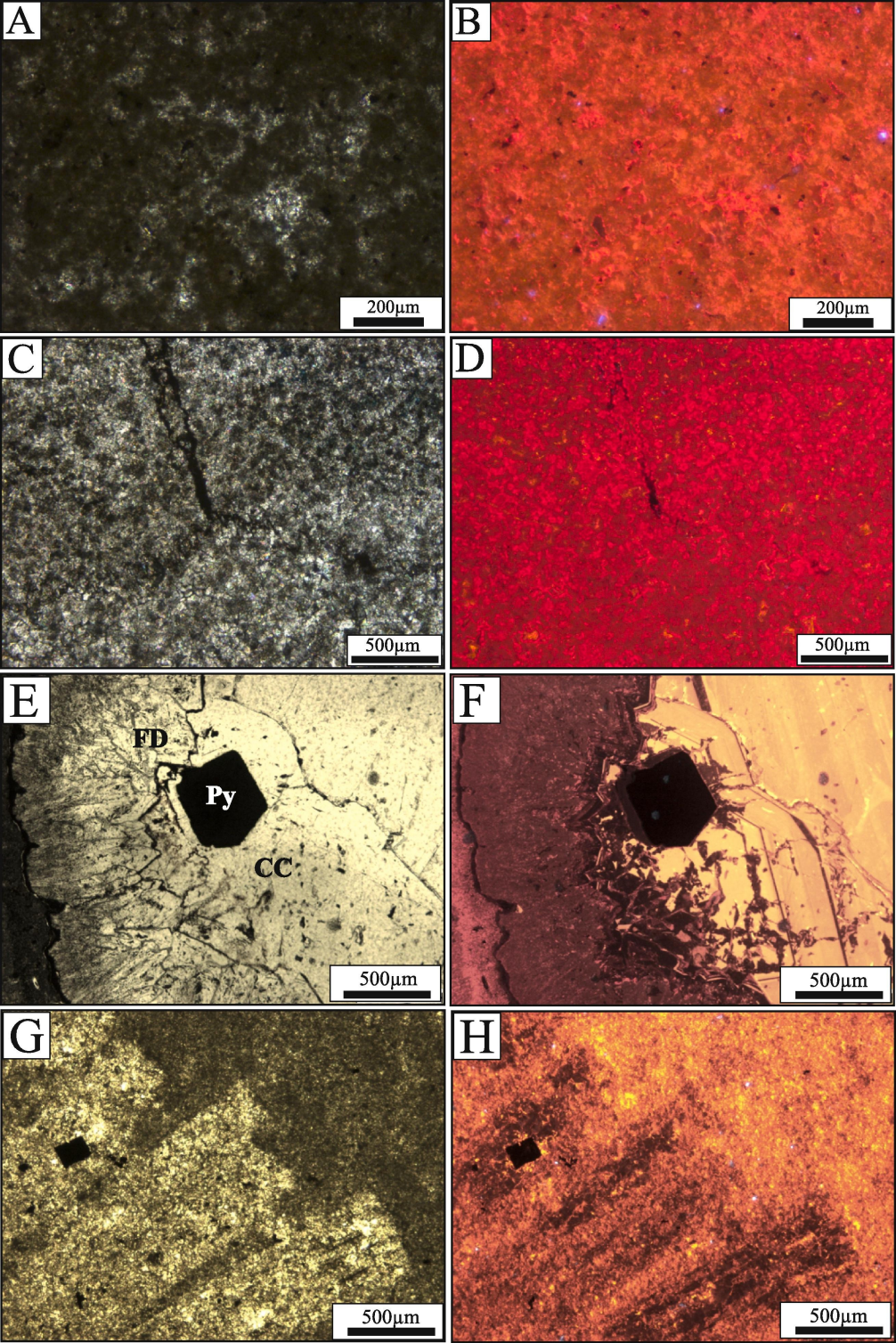
A
200μm
B
200μm
C
500μm
D
500μm
E
FD
Py
CC
500μm
F
500μm
G
500μm
H
500μm

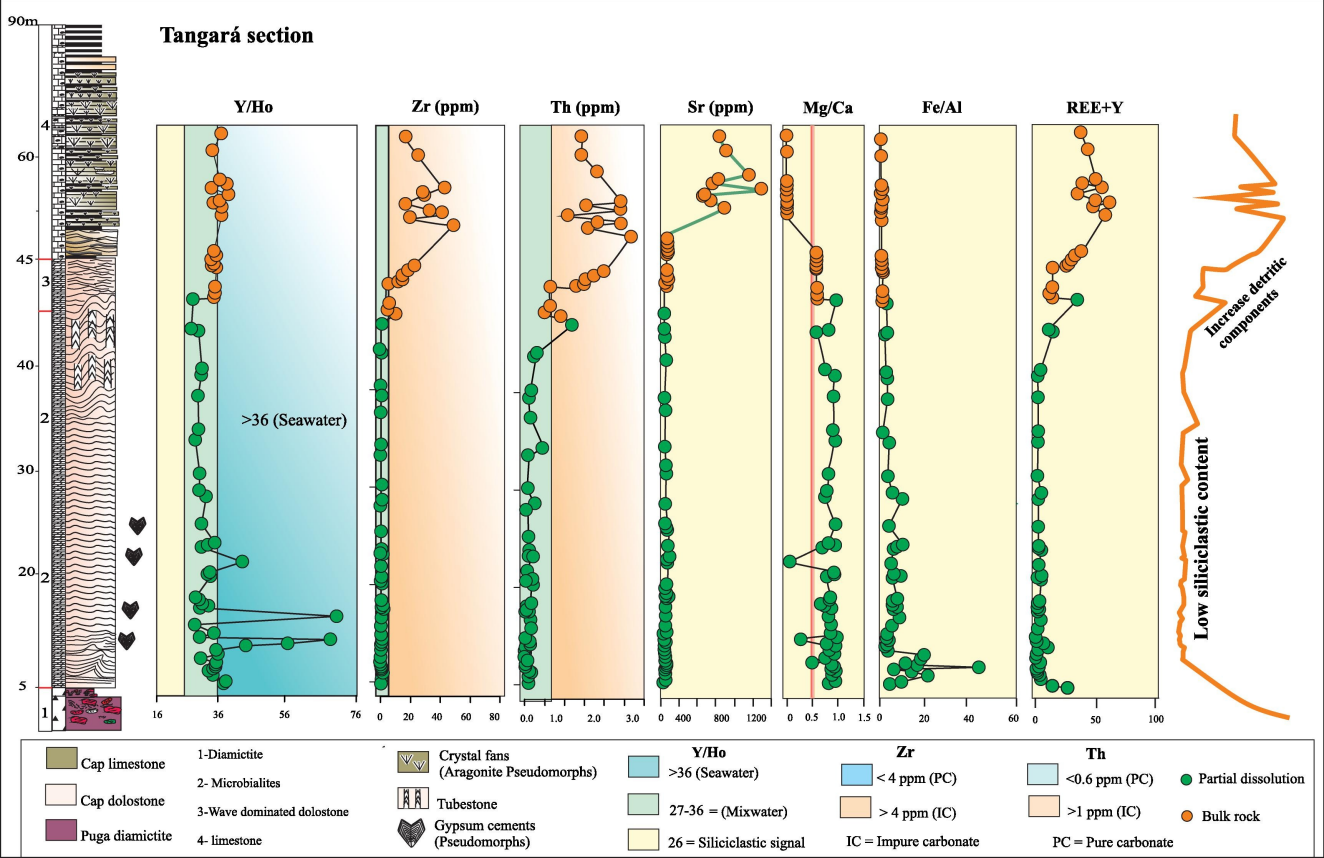
Tangará section
90m
Y/Ho
Zr (ppm)
Th (ppm)
Sr (ppm)
Mg/Ca
Fe/Al
REE+Y
>36 (Seawater)
Increase detritic components
Low siliciclastic content
16 36 56 76
0 20 40 60 80
0.0 1.0 2.0 3.0
0 400 800 1200
0 0.5 1.0 1.5
0 20 40 60
0 50 100
Cap limestone
Cap dolostone
Puga diamictite
1-Diamictite
2- Microbialites
3-Wave dominated dolostone
4- limestone
Crystal fans (Aragonite Pseudomorphs)
Tubestone
Gypsum cements (Pseudomorphs)
Y/Ho
>36 (Seawater)
27-36 = (Mixwater)
26 = Siliciclastic signal
Zr
< 4 ppm (PC)
> 4 ppm (IC)
IC = Impure carbonate
Th
<0.6 ppm (PC)
>1 ppm (IC)
PC = Pure carbonate
Partial dissolution
Bulk rock

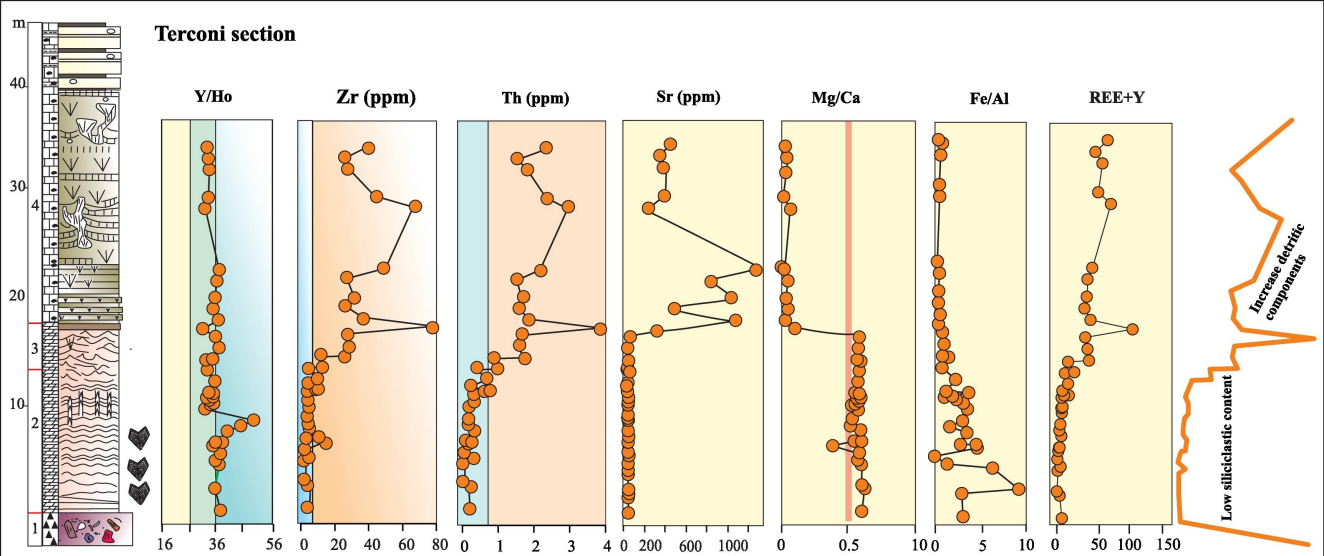
Terconi section
m
40
30
20
10
1
2
3
4
Y/Ho
Zr (ppm)
Th (ppm)
Sr (ppm)
Mg/Ca
Fe/Al
REE+Y
16 36 56
0 20 40 60 80
0 1 2 3 4
0 200 600 1000
0 0.5 10
0 5 10
0 50 100 150
Increase detritic components
Low siliciclastic content
Cap limestone
Cap dolostone
Puga diamictite
1-Diamictite
2- Microbialites
3-Wave dominated dolostone
4- limestone
Crystal fans (Aragonite Pseudomorphs)
Tubestone
Gypsum cements (Pseudomorphs)
Y/Ho
>36 (Seawater)
26-36(Mixwater)
25 = Siliciclastic signal
Zr
< 4 ppm (PC)
> 4 ppm (IC)
IC = Impure carbonate
Th
<0.6 ppm (PC)
>1 ppm (IC)
PC = Pure carbonate
Bulk rock

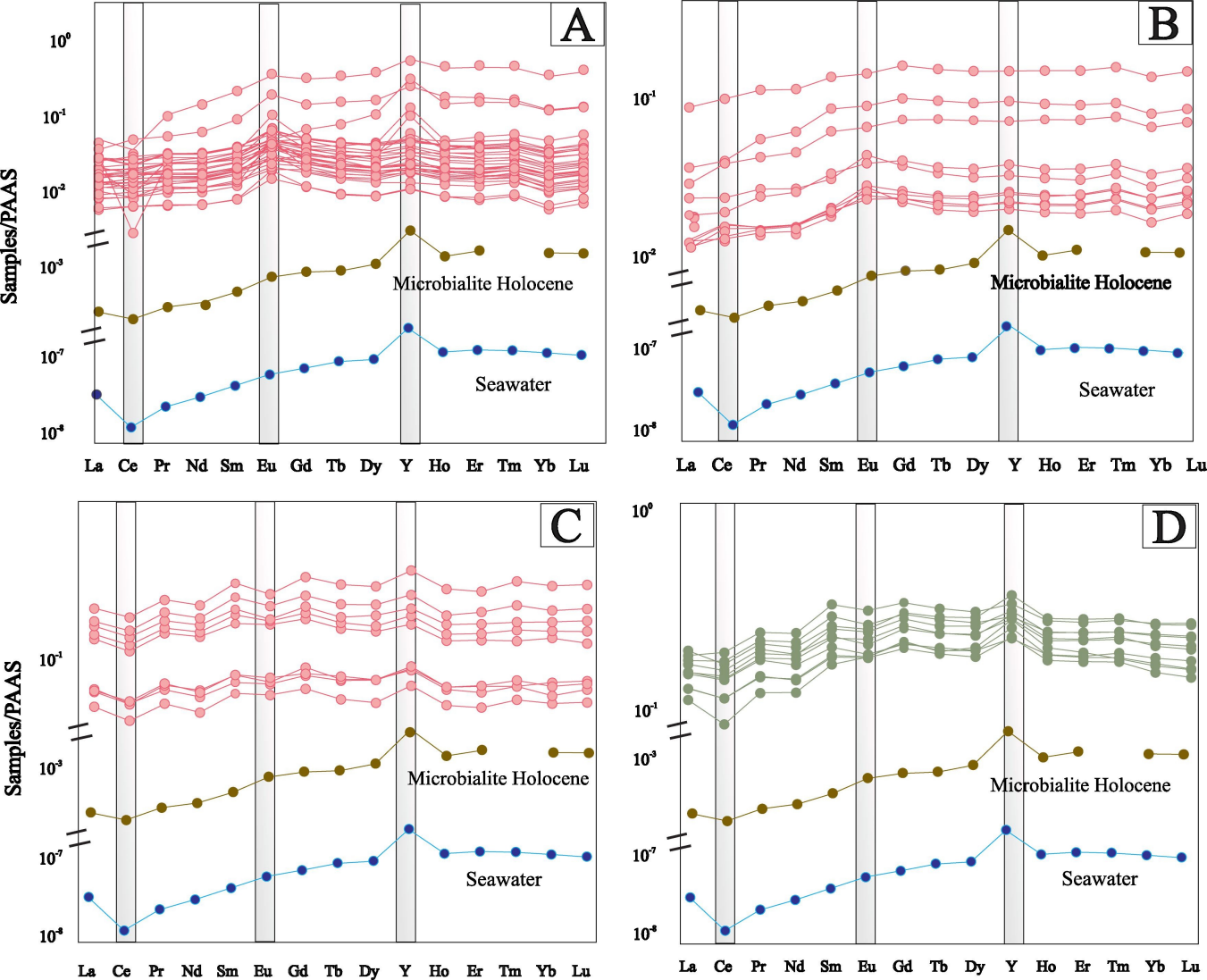
A
B
C
D
Samples/PAAS
Microbialite Holocene
Seawater
La Ce Pr Nd Sm Eu Gd Tb Dy Y Ho Er Tm Yb Lu

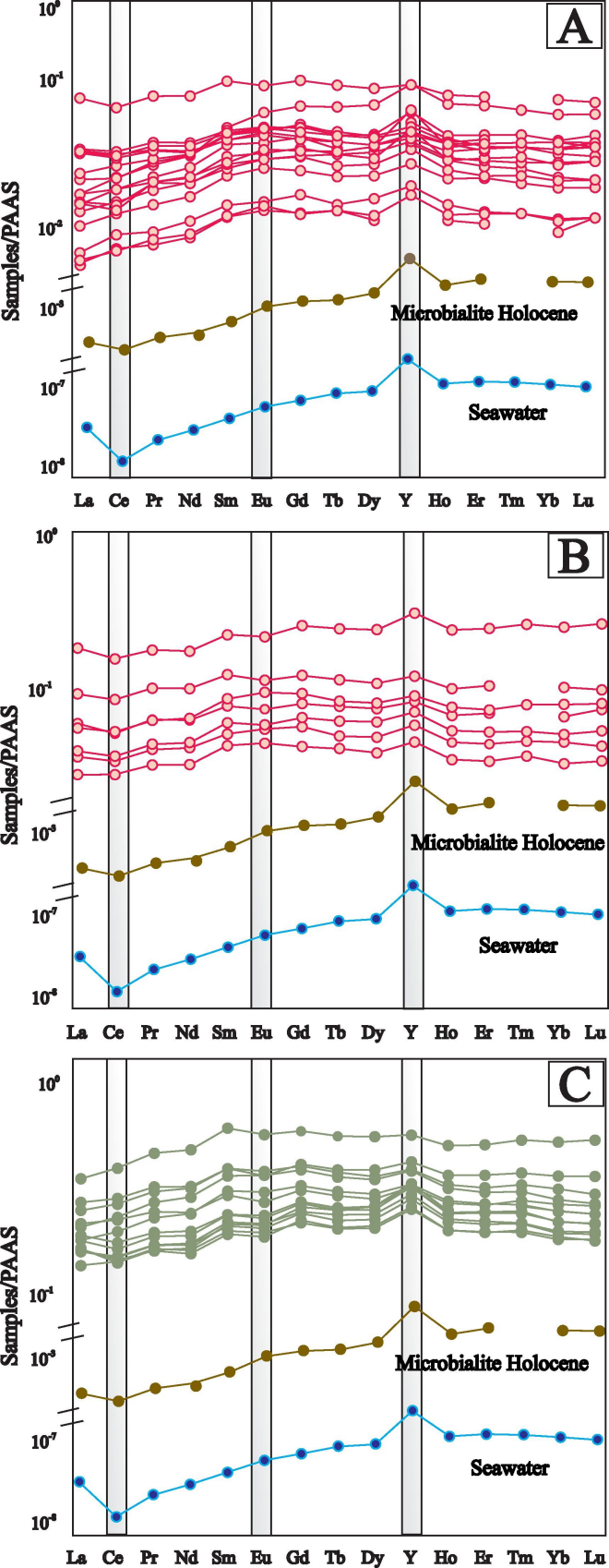
A
B
C
Samples/PAAS
Microbialite Holocene
Seawater
La Ce Pr Nd Sm Eu Gd Tb Dy Y Ho Er Tm Yb Lu

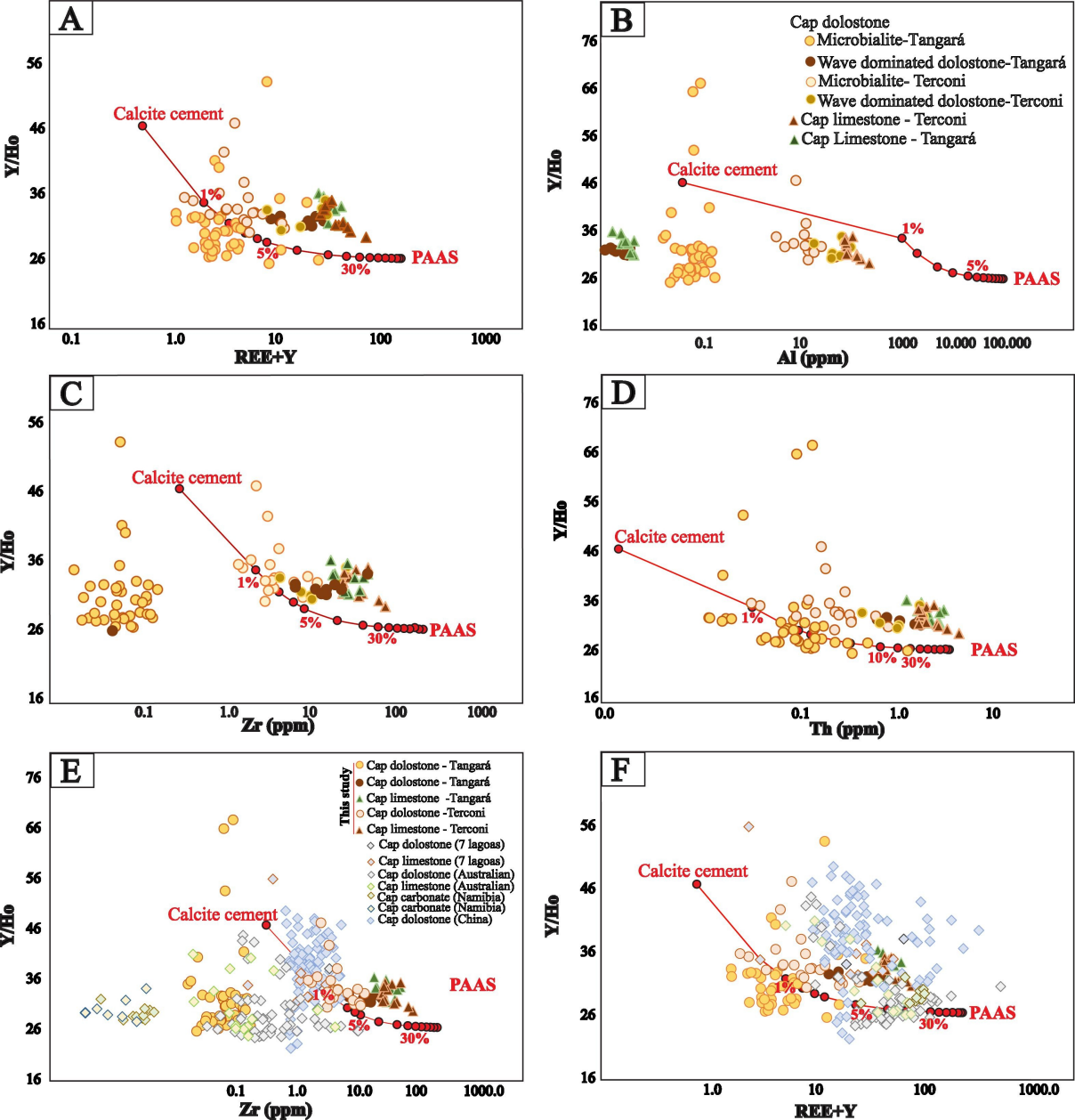
A
Y/Ho
REE+Y
Calcite cement
1%
5%
30%
PAAS
B
Cap dolostone
Microbialite-Tangará
Wave dominated dolostone-Tangará
Microbialite- Terconi
Wave dominated dolostone-Terconi
Cap limestone - Terconi
Cap Limestone - Tangará
Al (ppm)
C
Zr (ppm)
D
Th (ppm)
10%
E
This study
Cap dolostone - Tangará
Cap dolostone - Tangará
Cap limestone -Tangará
Cap dolostone -Terconi
Cap limestone - Terconi
Cap dolostone (7 lagoas)
Cap limestone (7 lagoas)
Cap dolostone (Australian)
Cap limestone (Australian)
Cap carbonate (Namibia)
Cap carbonate (Namibia)
Cap dolostone (China)
F

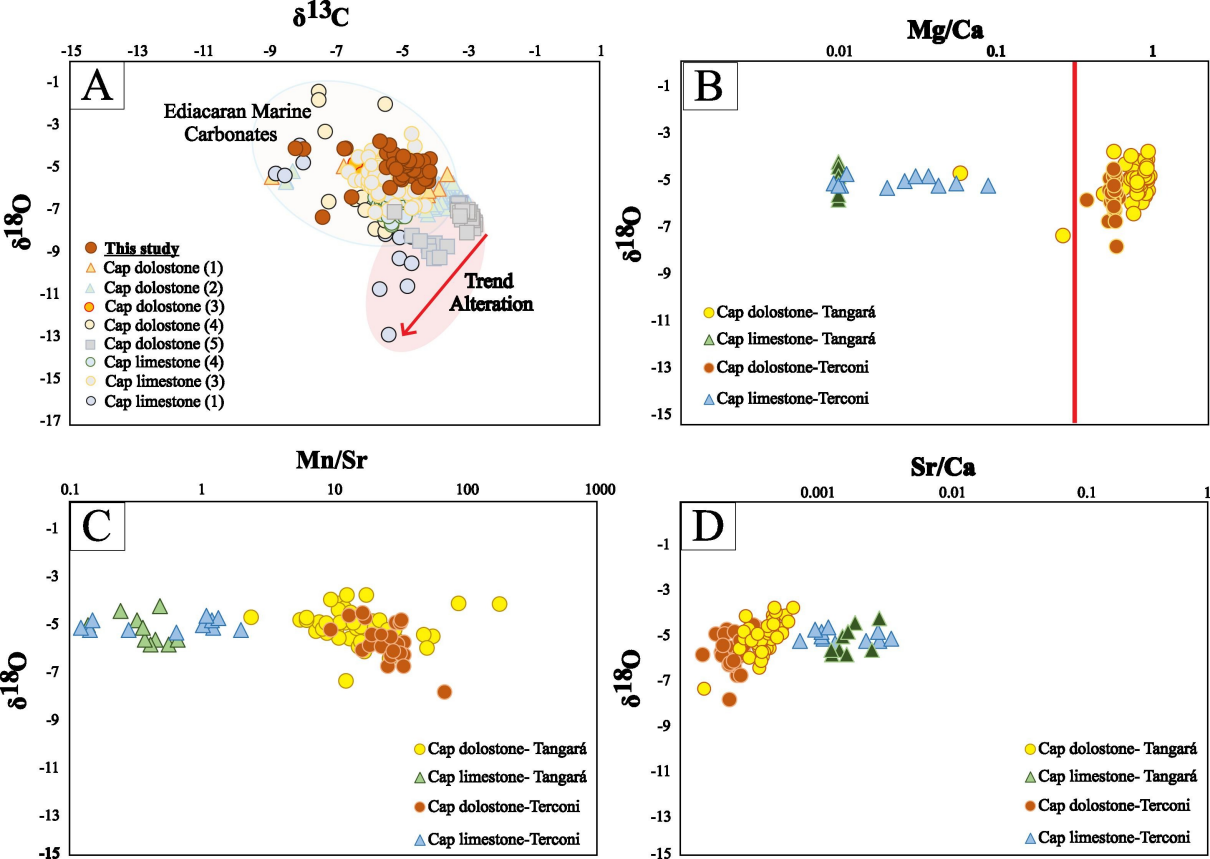
A
δ13C
δ18O
Ediacaran Marine Carbonates
Trend Alteration
This study
Cap dolostone (1)
Cap dolostone (2)
Cap dolostone (3)
Cap dolostone (4)
Cap dolostone (5)
Cap limestone (4)
Cap limestone (3)
Cap limestone (1)
B
Mg/Ca
δ18O
Cap dolostone- Tangará
Cap limestone- Tangará
Cap dolostone-Terconi
Cap limestone-Terconi
C
Mn/Sr
δ18O
Cap dolostone- Tangará
Cap limestone- Tangará
Cap dolostone-Terconi
Cap limestone-Terconi
D
Sr/Ca
δ18O
Cap dolostone- Tangará
Cap limestone- Tangará
Cap dolostone-Terconi
Cap limestone-Terconi

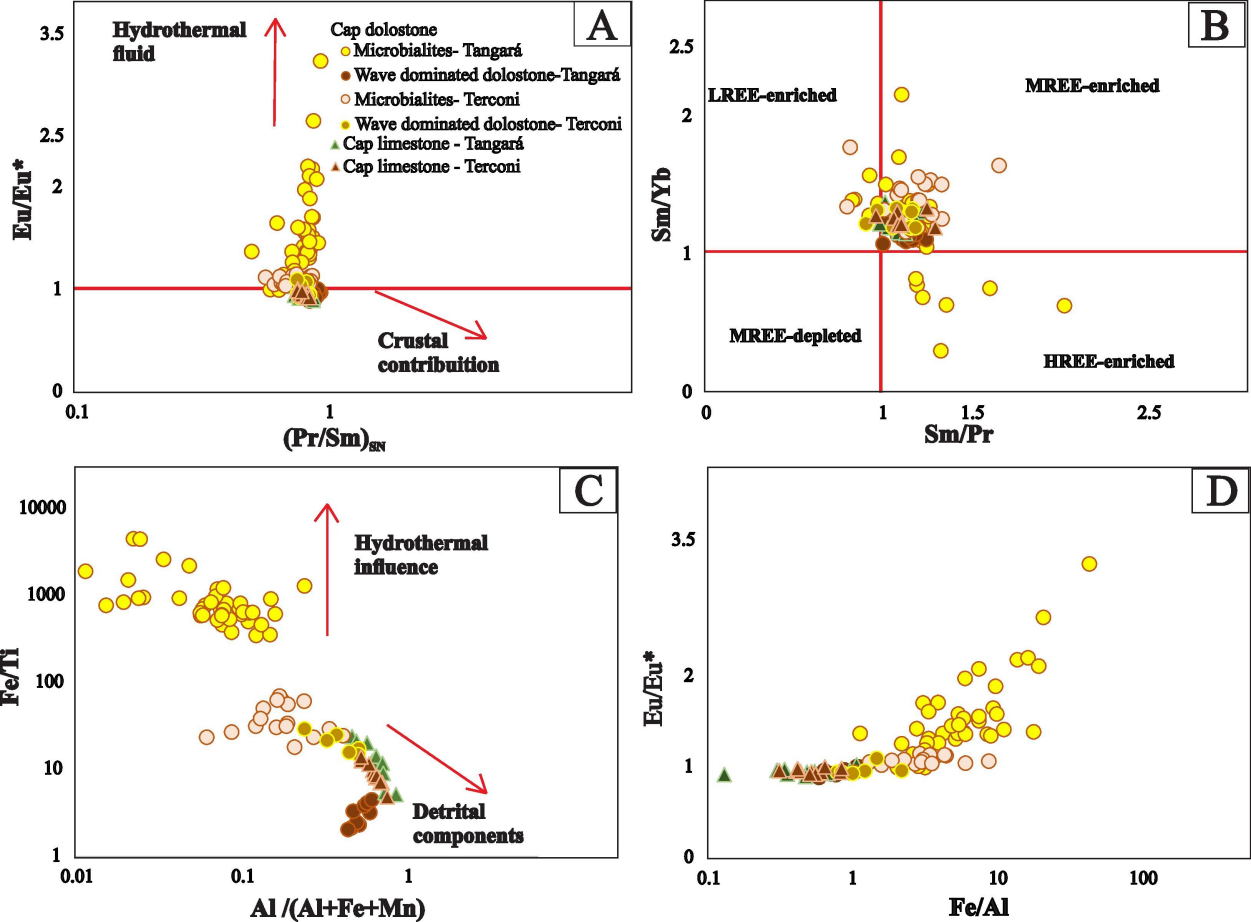
A
Hydrothermal fluid
Cap dolostone
Microbialites- Tangará
Wave dominated dolostone-Tangará
Microbialites- Terconi
Wave dominated dolostone- Terconi
Cap limestone - Tangará
Cap limestone - Terconi
Crustal contribuition
Eu/Eu*
(Pr/Sm)SN
B
LREE-enriched
MREE-enriched
MREE-depleted
HREE-enriched
Sm/Yb
Sm/Pr
C
Hydrothermal influence
Detrital components
Fe/Ti
Al /(Al+Fe+Mn)
D
Eu/Eu*
Fe/Al

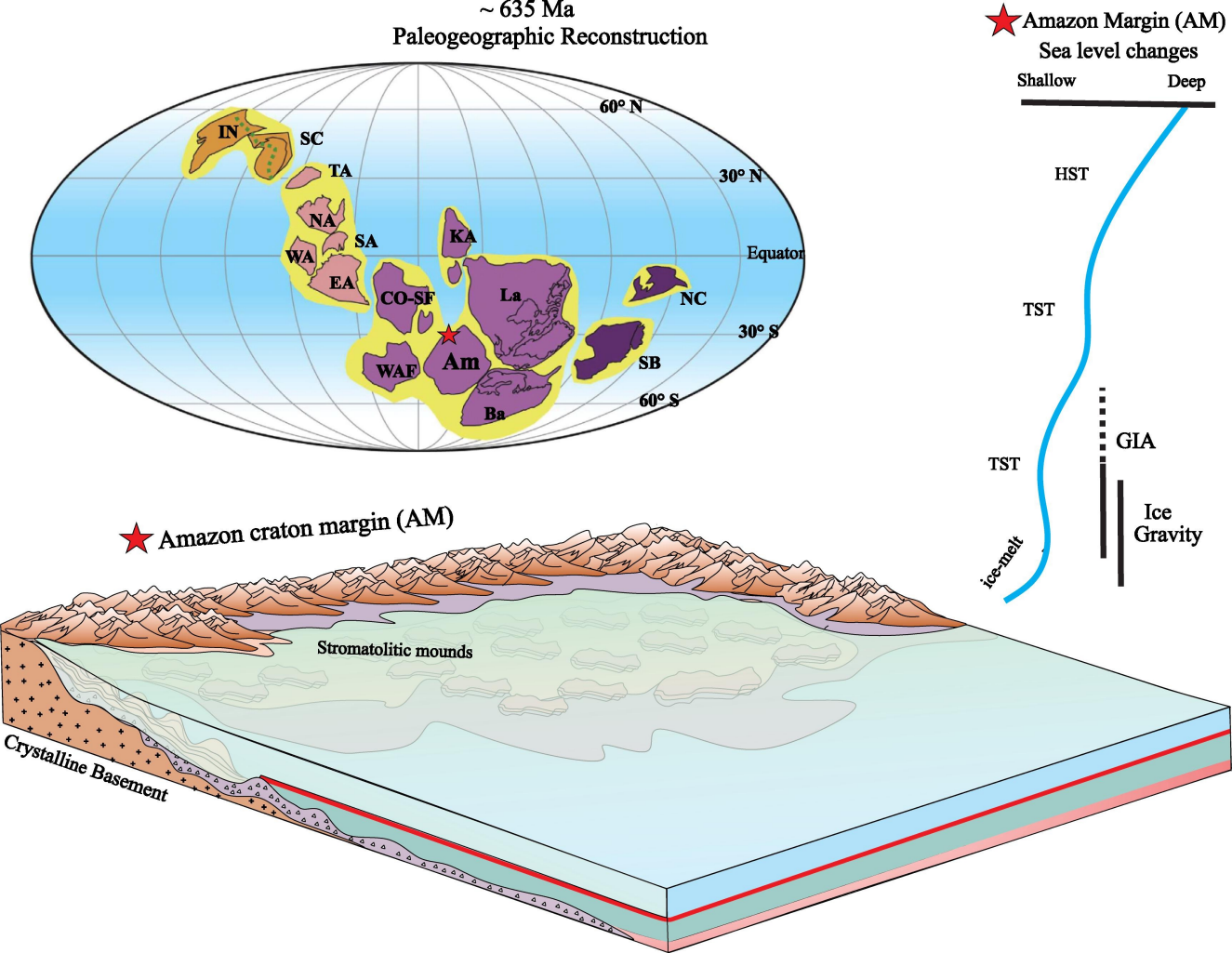
~ 635 Ma
Paleogeographic Reconstruction
60° N
30° N
Equator
30° S
60° S
IN
SC
TA
NA
SA
WA
EA
KA
CO-SF
La
NC
WAF
Am
SB
Ba
Amazon Margin (AM)
Sea level changes
Shallow
Deep
HST
TST
TST
GIA
Ice
Gravity
ice-melt
Amazon craton margin (AM)
Stromatolitic mounds
Crystalline Basement

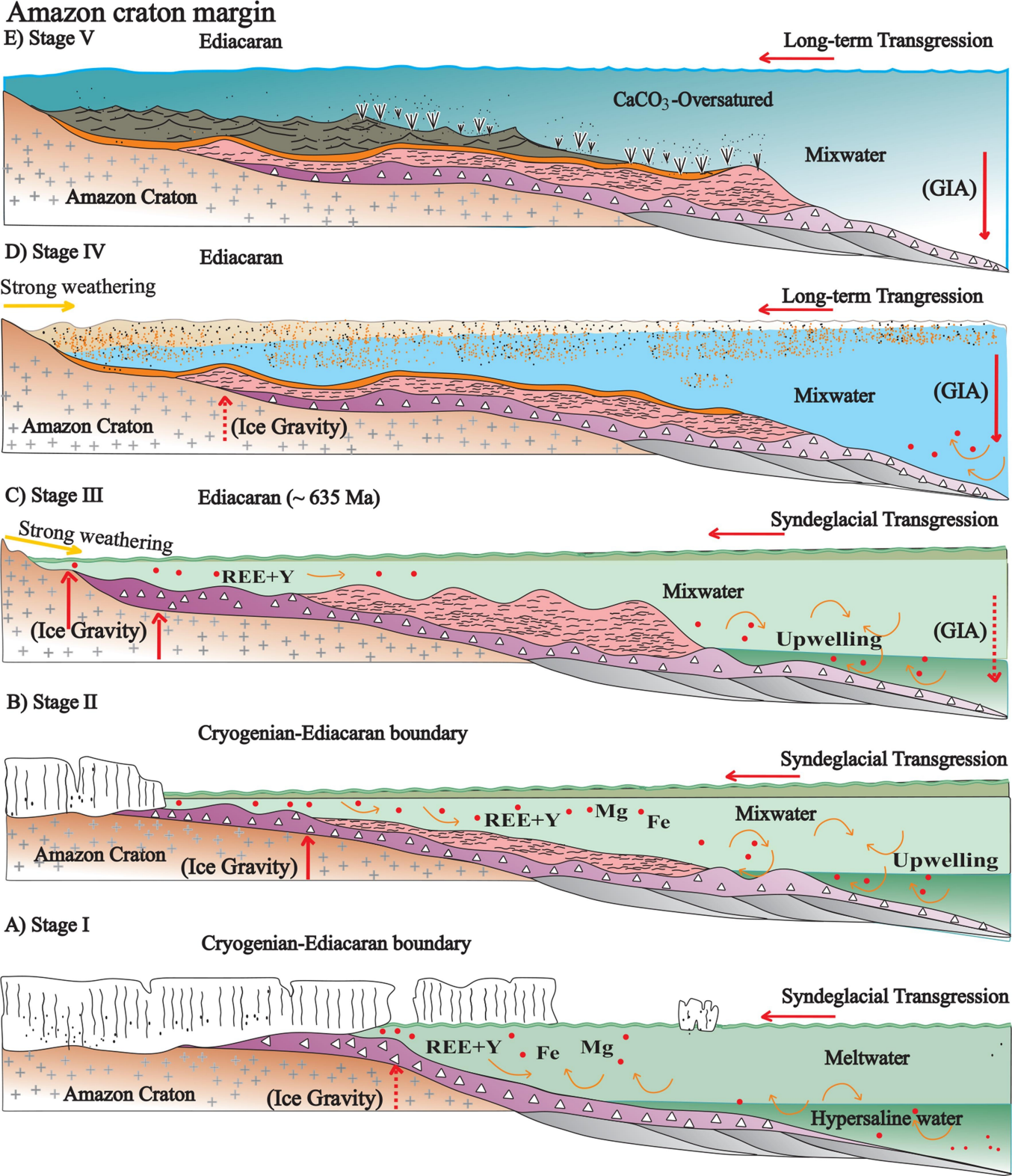
Amazon craton margin
E) Stage V
Ediacaran
Long-term Transgression
$CaCO_3$-Oversatured
Mixwater
(GIA)
Amazon Craton
D) Stage IV
Ediacaran
Strong weathering
Long-term Trangression
Mixwater
(GIA)
Amazon Craton
(Ice Gravity)
C) Stage III
Ediacaran (~ 635 Ma)
Syndeglacial Transgression
Strong weathering
REE+Y
Mixwater
(Ice Gravity)
Upwelling
(GIA)
B) Stage II
Cryogenian-Ediacaran boundary
Syndeglacial Transgression
REE+Y
Mg
Fe
Mixwater
Amazon Craton
(Ice Gravity)
Upwelling
A) Stage I
Cryogenian-Ediacaran boundary
Syndeglacial Transgression
REE+Y
Fe
Mg
Meltwater
Amazon Craton
(Ice Gravity)
Hypersaline water